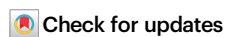


Probiotics functionalized with a gallium-polyphenol network modulate the intratumor microbiota and promote anti-tumor immune responses in pancreatic cancer

Received: 10 November 2023

Accepted: 12 August 2024

Published online: 17 August 2024


Zi-Yi Han¹, Zhuang-Jiong Fu¹, Yu-Zhang Wang¹ , Cheng Zhang¹, Qi-Wen Chen¹, Jia-Xin An¹ & Xian-Zheng Zhang¹  

The intratumor microbiome imbalance in pancreatic cancer promotes a tolerogenic immune response and triggers immunotherapy resistance. Here we show that *Lactobacillus rhamnosus* GG probiotics, outfitted with a gallium-polyphenol network (LGG@Ga-poly), bolster immunotherapy in pancreatic cancer by modulating microbiota-immune interactions. Upon oral administration, LGG@Ga-poly targets pancreatic tumors specifically, and selectively eradicates tumor-promoting *Proteobacteria* and microbiota-derived lipopolysaccharides through a gallium-facilitated disruption of bacterial iron respiration. This elimination of intratumor microbiota impedes the activation of tumoral Toll-like receptors, thus reducing immunosuppressive PD-L1 and interleukin-1 β expression by tumor cells, diminishing immunotolerant myeloid populations, and improving the infiltration of cytotoxic T lymphocytes in tumors. Moreover, LGG@Ga-poly hampers pancreatic tumor growth in both preventive and therapeutic contexts, and amplifies the antitumor efficacy of immune checkpoint blockade in preclinical cancer models in female mice. Overall, we offer evidence that thoughtfully designed biomaterials targeting intratumor microbiota can efficaciously augment immunotherapy for the challenging pancreatic cancer.

Cancer immunotherapy, particularly the treatment modality of immune checkpoint blockade (ICB), has shown remarkable efficacy across various tumor types^{1–5}. However, its impact on pancreatic ductal carcinoma (PDAC) - a malignancy notorious for its elevated fatality rate - has been noticeably limited⁶. This limitation predominantly arises from the profoundly immunosuppressive dynamics of the tumor microenvironment (TME)^{7–9}. This environment is distinguished by a substantial presence of tumor-associated

macrophages (TAMs) and myeloid-derived suppressor cells (MDSCs), paired with minimal infiltration of CD8⁺ cytotoxic T lymphocytes (CTLs)^{10,11}. Further, the tumor cells diminish their immunogenicity by undergoing antigenic loss or mutation, and by frequently attenuating the expression of major histocompatibility complex class I (MCH-I) molecules. This results in an impediment to the recognition and elimination of tumor cells by the immune system^{12,13}. Moreover, tumor-associated fibroblasts considerably

¹Key Laboratory of Biomedical Polymers of Ministry of Education & Department of Chemistry, Wuhan University, Wuhan 430072, P. R. China.

 e-mail: xz-zhang@whu.edu.cn

contribute to building physical barriers - primarily through collagen and chemokine secretion - this results in creating a dense extracellular matrix (ECM) that hinders T cell penetration into the core of PDA tumors¹⁴. These collective attributes of the TME advocate for the potential of enhancing PDAC immunotherapy by transitioning the existing immunosuppressive state towards a more immune-activated state. However, current strategies that target these tumor-associated components have made limited progress, underscoring the urgent need for other approaches to augment PDAC immunotherapy¹⁵.

Recent studies have revealed a notable increase in the presence of microbiota in cancerous pancreases compared to healthy ones¹⁶. Furthermore, the diversity of the intratumor microbiome significantly impacts the survival rates of individuals with pancreatic cancer¹⁷. This complex microbial environment interacts with the immune system, promoting immunotolerant pathways within the TME by expanding immunosuppressive immune cells such as TAMs and MDSCs¹⁸. Specifically, the elevated levels of *Proteobacteria* trigger chronic inflammation and induce PDA tumor cells to release interleukin-1 β (IL-1 β), which activates dormant pancreatic stellate cells (PSCs) and promotes ECM deposition. This creates an environment of TAM-mediated immunosuppression while impairing the infiltration and functionality of CD8⁺ T cells¹⁹. Moreover, persistent exposure to microbiota-derived lipopolysaccharides (LPS) leads to increased expression of programmed death ligand-1 (PD-L1) in tumor cells, directly compromising the effectiveness of ICB immunotherapy²⁰. In summary, dysregulation of intratumor microbiota in PDAC comprehensively shapes the landscape of tumor immunosuppression by affecting both immune cells and tumor cells. Strategically manipulating the PDA microbiome represents a crucial approach to reshape the tolerogenic innate and adaptive immune TME and enhance the efficacy of checkpoint-based immunotherapy.

In contrast to the extensively studied gut microbiota, the targeted modulation of intratumor microbiota remains largely unexplored²¹. Currently, antibiotics are commonly used to counteract the bacterial community within tumors²². However, routine antibiotic use for this purpose has drawbacks, as broad-spectrum antibiotics may induce bacterial resistance and inadvertently eliminate beneficial microbial

communities²³. Reduction in intratumor bacterial α -diversity and richness caused by antibiotics has been associated with shorter-term survival¹⁷. Additionally, the dense ECM of PDA tumors hampers antibiotic penetration, resulting in oral administration alone rarely reaching PDA tumors and potentially causing gut microbiota dysbiosis²⁴. To overcome these limitations and achieve more precise, effective, and safe modulation of the microbiota, other antimicrobials and delivery systems are urgently needed. Gallium, which mimics iron chemically, can disrupt bacterial iron metabolism and exhibit superior antimicrobial effects against various microbes²⁵. Targeting bacterial iron susceptibility with gallium also interferes with multiple iron-related metabolic processes crucial for bacterial survival²⁶. Consequently, the development of resistance to gallium among microbes occurs at a significantly slower rate²⁷. To facilitate the delivery of gallium into PDA tumors^{28–30}, we selected commercial *Lactobacillus rhamnosus* GG (LGG) which possess the ability to precisely target and infiltrate PDA tumors through the gut-pancreas axis following oral administration³¹. Furthermore, LGG can self-proliferate independently of iron sources, ensuring that gallium does not interfere with its bioactivity³².

Here, we show a strategy utilizing LGG probiotics armed with a gallium-polyphenol network and coated with chitosan nanocoating (LGG@Ga-poly) to modulate the intratumor microbiota and elicit anti-tumor immune response against PDAC (Fig. 1). Oral administration of LGG@Ga-poly selectively targets PDA tumors and effectively eliminates intratumor *Proteobacteria* and microbiome-derived LPS by inhibiting bacterial iron metabolism mediated by Ga³⁺. This process inhibits the activation of Toll-like receptors (TLRs) dependent on microbial presence, leading to a reversal of the immunosuppressive TME. It results in a reduction in immunotolerant myeloid populations and enhanced recruitment of T cells. Notably, LGG@Ga-poly demonstrates significant delay in tumor initiation in a preventive setting and shows potential as an independent therapy or in combination with checkpoint-based immunotherapy for established PDA tumors. This biohybrid material effectively and safely modulates the intratumor microbiome, enhancing the overall efficacy of ICB immunotherapy for challenging PDAC³³.

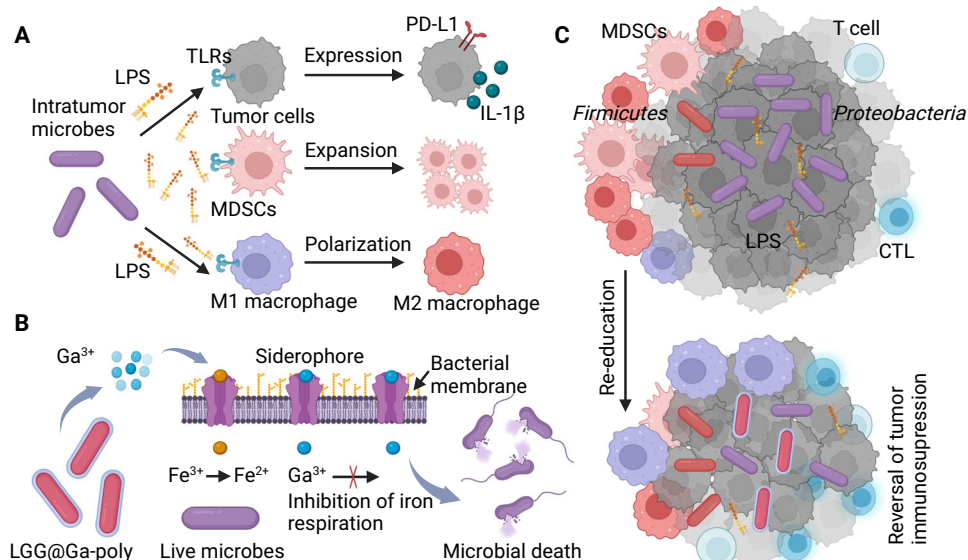


Fig. 1 | Schematic illustration of LGG@Ga-poly for PDA immune activation through modulation of intratumor microbiota. **A** Intratumor microbes and their metabolite LPS induce PDA immunosuppression. Microbiota-derived LPS activates TLRs expressed by tumor cells, MDSCs, and macrophages, promoting the expression of PD-L1 and secretion of IL-1 β by tumor cells and the expansion of immunotolerant myeloid populations. **B** LGG@Ga-poly eliminates intratumor bacteria and

LPS by Ga³⁺-mediated disruption of bacterial iron respiration. **C** LGG@Ga-poly inhibits LPS-dependent TLR activation, thus reducing MDSC populations, polarizing M2-like macrophages into M1-like types and improving tumor-infiltrating CD8⁺ cytotoxic T lymphocytes (CTLs). Figure 1, created with BioRender.com, released under a Creative Commons Attribution-NonCommercial-NoDerivs 4.0 International license.

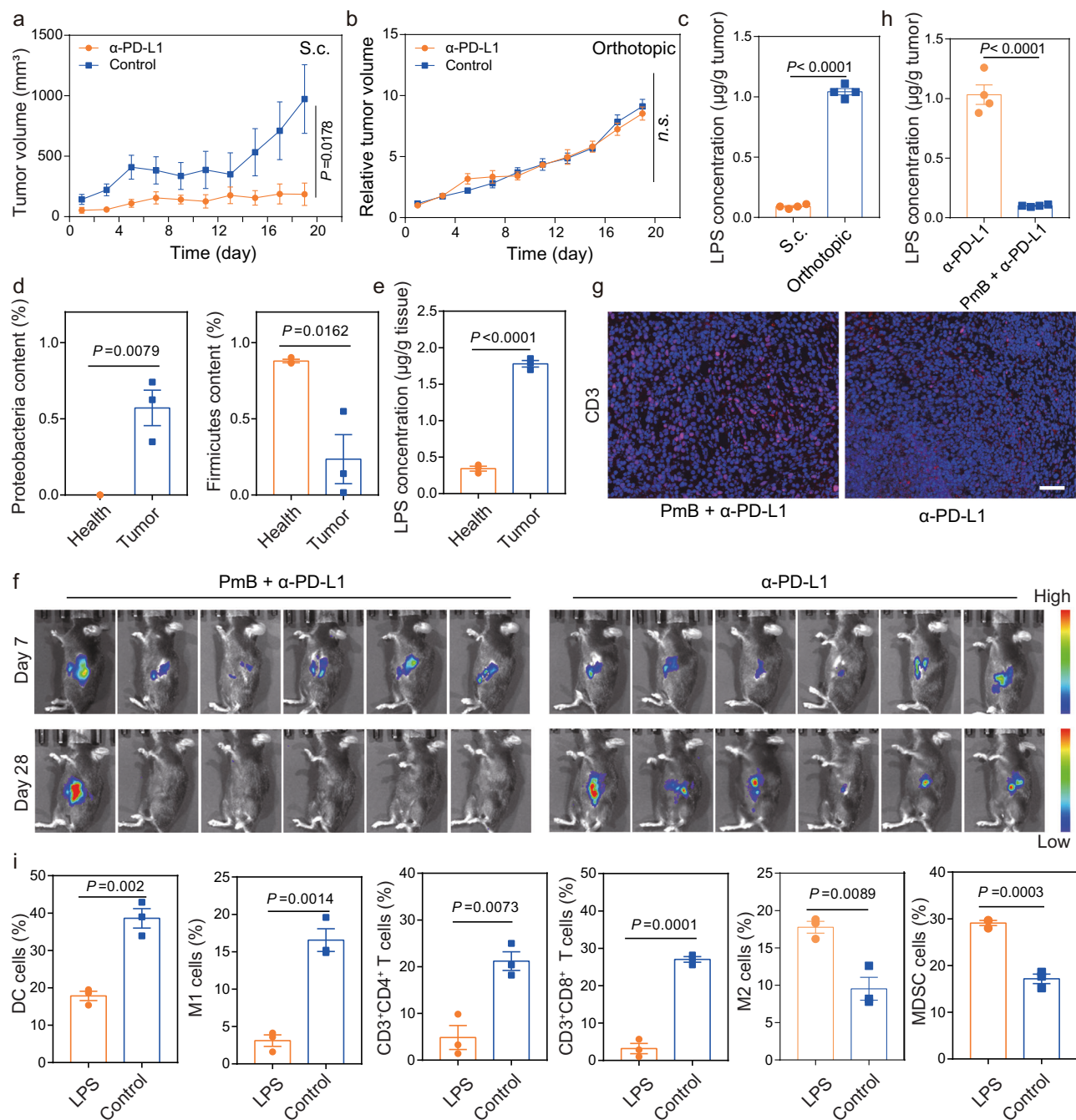


Fig. 2 | Intratumor microbiota induced PDA TME immunosuppression and restrained α-PD-L1 immunotherapy efficacy. **a** Subcutaneous (S.c.) tumor and **b** orthotopic tumor growth curves after α-PD-L1 treatment ($n = 9$ mice). **c** Concentration of LPS in S.c. and orthotopic PDA tumors ($n = 4$ samples). Content of **d** *Proteobacteria*, *Firmicutes* bacteria, and **e** LPS in pancreatic tumors and healthy pancreatic tissues ($n = 3$ samples). **f** Bioluminescence images of orthotopic PDAC mice treated with α-PD-L1 or α-PD-L1 plus polymyxin B (PmB) ($n = 6$ mice). **g** Immuno-fluorescence staining of intratumor T cell infiltration treated with α-PD-

L1 or α-PD-L1 plus PmB. The scale bar is 50 μm. Experiments were performed three times with similar results ($n = 6$ mice). **h** Concentration of LPS in tumors treated with α-PD-L1 or α-PD-L1 plus PmB ($n = 4$ samples). **i** Infiltration of intratumor immune cells in PDA tumors with and without LPS stimulation ($n = 3$ samples). Significance between two groups was calculated using two-tailed Student's *t*-tests (**a–e**, **h**, and **i**). Data are means \pm sem. *n.s.* means no significance. Source data are provided as a Source Data file.

Results

Intratumor microbiota dysbiosis induces PDAC immunosuppression

Firstly, we evaluated the therapeutic effectiveness of ICB in subcutaneous and orthotopic murine models using Panc-02 cells. We observed that anti-PD-L1 (α-PD-L1) treatment significantly suppressed tumor growth in subcutaneous tumors but showed no inhibition in orthotopic tumors (Fig. 2a, b). Immunofluorescence staining revealed

a higher population of T cells in subcutaneous tumors compared to orthotopic tumors (Supplementary Fig. 1a). The distinct response to ICB was unlikely due to genetic factors as the cell line and mouse strain were identical³⁴. Recognizing the importance of host-microbe interactions in immune modulation³⁵, we hypothesized that intratumor microbes might be responsible for inducing resistance to PDAC immunotherapy. To test this hypothesis, we analyzed the profiles of intratumor microbiota in the two tumor models. Fluorescence in situ

hybridization (FISH) assays confirmed a substantial presence of microbes in orthotopic tumors, in contrast to subcutaneous tumors (Supplementary Fig. 1b). Furthermore, elevated levels of microbiota-derived LPS were detected in orthotopic tumors, while minimal LPS was observed in subcutaneous tumors (Fig. 2c).

To confirm the contribution of intratumor microbiota to the unresponsiveness of PDA to α -PD-L1 therapy, we investigated the potential of antibiotics to restore responsiveness to checkpoint-based immunotherapy. Initially, we compared the microbiota profiles between normal and cancerous pancreases using 16S rDNA gene sequencing³⁶. The analysis revealed a significant increase in *Proteobacteria* and a decrease in *Firmicutes* in PDA tumors compared to normal pancreases (Fig. 2d and Supplementary Fig. 2a). Moreover, the intratumor content of LPS was significantly higher in PDA tumors than in normal pancreases (Fig. 2e). When combined with polymyxin B (PmB)³⁷, an antimicrobial peptide that inactivates LPS-expressing bacteria, the antitumor efficacy of α -PD-L1 treatment improved significantly (Fig. 2f). The combination therapy of PmB and α -PD-L1 resulted in durable tumor regression and increased infiltration of T cells (Fig. 2f, g). Correspondingly, there was a notable reduction in bacterial load in the antibiotic-treated group, accompanied by a significant decrease in LPS levels (Fig. 2h and Supplementary Fig. 2b). The LSL-KrasG12D-Pdx1-Cre (KPC) transgenic mouse model closely replicates many features of human pancreatic cancer, and we found that antibiotic treatment in this model also significantly enhanced the efficacy of α -PD-L1 (Supplementary Fig. 3a).

To gain a more comprehensive understanding of the role of intratumor microbiota in immune suppression in PDAC, we conducted experiments to investigate whether microbiota within the TME triggers immunosuppression through the production of LPS, a metabolite derived from the microbiota. We co-inoculated LPS and tumor cells directly into the pancreas of mice and collected PDA tumors after four weeks for histological analysis. Hematoxylin-eosin (H&E) staining revealed that LPS promoted tumor growth, while immunofluorescence staining indicated an increase in intratumor α -smooth muscle actin (α -SMA) and Collagen I content³⁸, suggesting heightened inflammation within the tumor (Supplementary Fig. 3b, c). Additionally, we collected immune cells from tumors and lymph nodes for flow cytometry (FCM) analysis. The presence of LPS led to a significant decrease in antigen-presenting cells (APCs), including mature dendritic cells (DCs) and M1-like macrophages with antitumor properties. Notably, there was a notable increase in the proportions of M2-like macrophages and MDSCs after LPS treatment. Furthermore, the percentage of cytotoxic CD8⁺ T cells, which play a crucial role in antitumor immunity, was reduced in the LPS-treated group (Fig. 2i). In vitro assays demonstrated that LPS did not directly affect the growth and migration of PDA tumor cells (Supplementary Fig. 4). Overall, these findings provide evidence that intratumor microbiota, particularly microbial LPS, mediates tumor immunosuppression in PDAC and contributes to resistance against ICB immunotherapy.

Preparation and characterization of LGG@Ga-poly

To eliminate intratumor microbiota, we utilized LGG probiotics to promote the targeting and penetration of bacteria-inactivated Ga³⁺ into the tumors (Fig. 3a). After screening various antibacterial metal ions, we identified Ga³⁺ as an effective agent for inactivating multiple microbes while causing minimal toxicity to LGG (Fig. 3b and Supplementary Fig. 5). Functionally, Ga³⁺ eliminates microbes by mimicking iron ions and disrupting iron-related metabolic pathways within bacteria. Interestingly, the metabolism of LGG is not dependent on iron, rendering it resistant to inactivation by Ga³⁺ (Supplementary Fig. 6)³⁹. Next, we coated LGG with a biocompatible supramolecular coating composed of Ga³⁺ and plant polyphenols. We screened three kinds of polyphenols⁴⁰, including tannin (TA), gallic acid (GA), and epigallocatechin gallate (EGCG), and found that the antibacterial activity of Ga³⁺

for *Escherichia coli* was enhanced when coordinated with polyphenols (Fig. 3c). The bacterial carrier for iron uptake, known as siderophore⁴¹, is a polyphenolic structure, suggesting that the gallium-polyphenol coordination can improve Ga³⁺ endocytosis within bacterial cells. This hypothesis was confirmed by inductively coupled plasma (ICP) measurement, with more Ga³⁺ being detected in bacteria in the presence of polyphenols (Supplementary Fig. 7). When Ga³⁺ was combined with EGCG, the most bacterial death was observed. Therefore, we self-assembled a gallium-EGCG network as a single-cell nanocoating to encapsulate probiotic cells. To prevent the premature leakage of Ga³⁺ in the gastrointestinal (GI) tract, we further deposited positively charged chitosan films by electrostatic cross-linking to form LGG@Ga-poly.

The changes in zeta potentials of LGG confirmed the successful deposition of each layer (Fig. 3d). Both scanning electron microscopy (SEM) and transmission electron microscopy (TEM) observations indicated that LGG@Ga-poly displayed a distinct polymer layer around bacterial cells (Supplementary Fig. 8). TEM-assisted element mapping of C, O, and Ga elements confirmed that the Ga-based polymer layers were located on the bacterial cell surface (Fig. 3e). After Ga-poly deposition, the solutions darkened, and correspondingly, the UV-visible spectrum was changed (Supplementary Fig. 9). Furthermore, Ga-EGCG and chitosan did not inhibit LGG growth and bioactivity (Fig. 3f). We evaluated the tolerance capacity of LGG@Ga-poly in different conditions, including simulated gastric fluid (SGF) and simulated colonic fluid (SCF). The viability of LGG@Ga-poly was not significantly affected after treatment with SGF and SCF, as shown in Fig. 3g and Supplementary Fig. 10a. The loading efficacy of Ga³⁺ was determined as 56.7%, and the chitosan deposition effectively prevented Ga³⁺ leakage in the SGF (Fig. 3h). This feature is beneficial in reducing fluctuations in the gut microbiota, thereby enhancing biosafety.

Next, we evaluated the antibacterial and LPS-scavenging abilities of LGG@Ga-poly. LGG alone exhibited a slight inhibitory effect on bacterial growth due to nutrient competition and metabolic antagonism. In contrast, LGG@Ga-poly effectively inhibited the growth of bacteria such as *E. coli*, *Staphylococcus aureus* (*S. aureus*), and cancer-promoting *Fusobacterium nucleatum* (*F. nucleatum*), which are commonly found in PDA tumors (Fig. 3i and Supplementary Fig. 10b, c). Bacterial plate counting further confirmed the superior antimicrobial behavior of LGG@Ga-poly (Supplementary Fig. 10d). Then, we constructed a *F. nucleatum*-infected Panc-02 cell model to investigate the antibacterial ability of materials for intracellular bacteria, and the results showed that both Ga³⁺ and LGG@Ga-poly could inhibit intracellular bacterial growth (Supplementary Fig. 10e). The addition of exogenous Fe³⁺ significantly inhibited the antibacterial effect of LGG@Ga-poly, indicating that LGG@Ga-poly kills bacteria by disrupting bacterial iron metabolism (Fig. 3j).

The dense ECM in PDA tumors hinders the penetration of free antimicrobials, resulting in their retention in the intestines. This can disrupt the balance of gut microbiota and lead to unintended side effects. To investigate whether LGG@Ga-poly can overcome these biological barriers in PDA tumors, we established a 3D tumor sphere infected with *E. coli* for in vitro experiments. As shown in Supplementary Fig. 11a, free Cy5 was only observed in the outermost layer of the tumor sphere, while LGG modified with Cy5 (LGG@Cy5) effectively penetrated the entire tumor sphere. Leveraging the natural active mobility of bacteria and their hypoxia-tropism behavior, LGG@Cy5 reached deeper, hypoxic tumor regions. Furthermore, LGG@Ga-poly delivered more Ga³⁺ to the tumor spheres compared to the group treated with free Ga³⁺ (Supplementary Fig. 11b). LGG@Ga-poly also exhibited enhanced penetration in the *E. coli*-infected tumor spheres (Fig. 3k). As expected, Ga³⁺ alone did not significantly inhibit bacterial growth, while LGG@Ga-poly effectively eliminated both microbes and LPS in the tumor spheres (Fig. 3l).

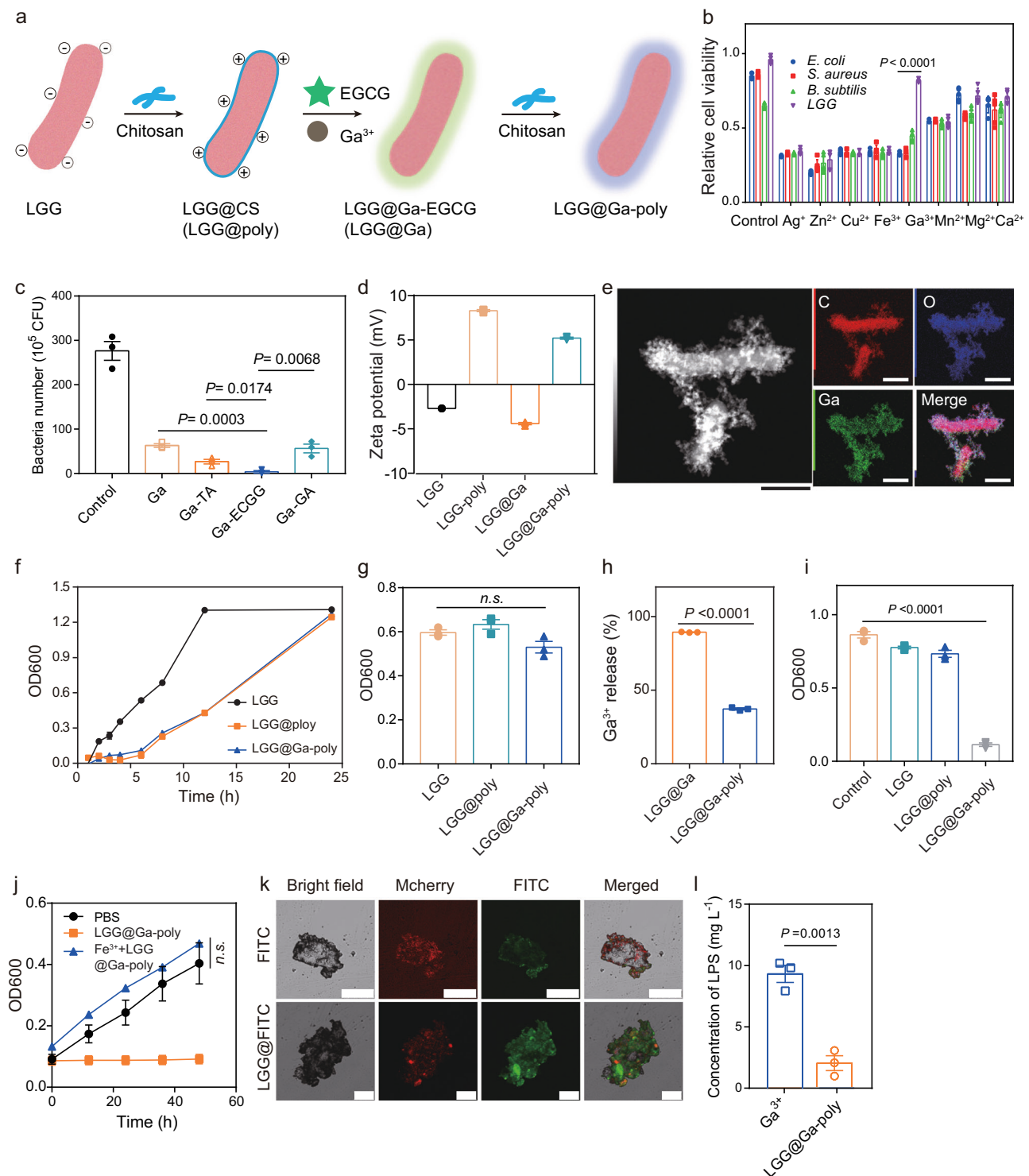


Fig. 3 | Preparation and in vitro antimicrobial behavior of LGG@Ga-poly.

a Schematic illustration of the preparation of biohybrid LGG@Ga-poly. **b** Screening for different ions with antimicrobial properties evaluated on *E. coli*, *S. aureus*, *B. subtilis*, and LGG ($n = 5$ samples). **c** Number of *E. coli* colonies after treatment with Ga^{3+} or Ga^{3+} coordinated with different polyphenols ($n = 3$ samples). **d** Zeta potentials of different materials, including LGG, LGG coated with chitosan (LGG-poly), LGG-poly coated with Ga-EGCG (LGG@Ga), and LGG@Ga-poly ($n = 3$ samples). **e** TEM-assisted element mapping of LGG@Ga-poly (C element; O element; Ga element). The scale bars are 1 μm . Experiments were performed three times. **f** Growth curves of LGG, LGG@poly, and LGG@Ga-poly in MRS medium ($n = 5$ samples). **g** LGG viability in the simulated gastric fluid (SGF) treated with different materials, including LGG, LGG@poly, and LGG@Ga-poly ($n = 3$ samples).

h Ga^{3+} release in simulated colonic fluid (SCF) of LGG@Ga and LGG@Ga-poly ($n = 3$ samples). **i** The growth of *F. nucleatum* after different treatments ($n = 3$ samples). **j** The growth of *E. coli* after treatment by LGG@Ga-poly or LGG@Ga-poly plus Fe^{3+} ($n = 6$ samples). **k** Penetration of FITC or LGG@FITC into PDAC 3D cell spheres. The cell spheres were pre-infected with Mcherry-expressing *E. coli*. Mcherry-field images, FITC-field images, and merged images are shown. The scale bars are 50 μm . Experiments were repeated three times. **l** Concentration of LPS in cell spheres treated with free Ga^{3+} or LGG@Ga-poly ($n = 3$ samples). Significance between two groups was calculated using two-tailed Student's t-tests (**h** and **l**) or one-way ANOVA with Tukey post hoc test (**b**, **c**, **g**, **i**, and **j**). Data are means \pm sem. *n.s.* means no significance. Source data are provided as a Source Data file.

In vivo modulation of intratumor microbiota by LGG@Ga-poly
Initially, we assessed the biodistribution of LGG@Ga-poly in an orthotopic Panc-02-bearing mouse model following oral administration. LGG@Ga-poly, labeled with Cy5.5, was tracked using the in vivo imaging system (IVIS) for whole-body fluorescence imaging of mice. Fluorescence signals were observed in tumor areas as early as 2 hours post-administration, reaching a peak at 8 hours and maintaining strong intensity even after 7 days. Ex vivo fluorescence imaging of tumors and major organs further confirmed the promising tumor-targeting capability of LGG@Ga-poly (Fig. 4a and Supplementary Fig. 12a). Histological imaging demonstrated specific accumulation of LGG@Ga-poly within tumor tissues, while minimal accumulation was observed in normal organs (Supplementary Fig. 12b). Moreover, the concentration of Ga³⁺ in tumors was higher compared to major organs (Fig. 4b). Photoacoustic imaging (PAI) revealed that tumors treated with LGG@Cy5.5 exhibited a more pronounced photoacoustic signal compared to tumors treated with free Cy5.5, indicating enhanced tumor penetration of the antimicrobials facilitated by the LGG (Fig. 4c).

Subsequently, we evaluated the in vivo modulation of intratumor microbiota by LGG@Ga-poly. At the end of the treatment, orthotopic tumors were collected for analysis of intratumor microbiota. No significant difference in operational taxonomic units (OTUs) was observed between the control and LGG@Ga-poly treatment groups (Fig. 4d). The α -diversity of intratumor microbiota, as measured by the Simpson diversity index, remained unchanged (Fig. 4e). However, LGG@Ga-poly treatment induced a distinct clustering of the microbial community structure, as indicated by principal components analysis (PCA) reflecting β -diversity (Fig. 4f). Analysis at the phylum level demonstrated that LGG@Ga-poly treatment significantly reduced the abundance of *Proteobacteria*, a group of bacteria associated with pro-tumoral effects (Fig. 4g and Supplementary Fig. 13). At the genus level, *Lactobacillus* richness was notably enhanced following LGG@Ga-poly treatment, suggesting successful niche competition (Fig. 4h). Furthermore, the overall bacterial load within tumors decreased after LGG@Ga-poly treatment (Fig. 4i). Correspondingly, the concentration of LPS within tumors treated with LGG@Ga-poly was approximately 5-fold lower compared to tumors treated with PBS (Fig. 4j).

A compromised intestinal barrier can lead to the infiltration of bacterial LPS from the gut into the bloodstream and tumor tissues, exacerbating tumor immunosuppression. To address this concern, we thoroughly evaluated the impact of LGG@Ga-poly treatment on both gut microbiota and intestinal barrier function. Our assessment revealed that oral administration of LGG@Ga-poly minimally affected gut microbiota homeostasis, as evidenced by no significant changes in bacterial OTUs, α -diversity, or phylum-level diversity (Supplementary Fig. 14). Additionally, the concentration of LPS in the gut did not show any significant changes following different treatments (Fig. 4k). To assess intestinal barrier integrity, an in vivo intestinal permeability assay using FITC-dextran was conducted⁴². The results demonstrated a remarkable 2-fold decrease in FITC concentration in the blood after treatment with LGG@Ga-poly, indicating the restoration of intestinal barrier function (Fig. 4l). Consequently, LGG@Ga-poly treatment resulted in a significant threefold decrease in detected blood levels of LPS compared to the PBS-treated group (Fig. 4m). In conclusion, we have demonstrated that oral administration of LGG@Ga-poly effectively eliminates intratumor microbiota and microbiota-derived LPS, while concurrently restoring intestinal homeostasis to mitigate LPS leakage into the bloodstream (Fig. 4n).

In vivo antitumor responses

Firstly, we evaluated the therapeutic effect of different materials in a prophylactic setting. Healthy C57BL/6 mice were pretreated with different materials, including PBS, LGG, Ga-poly, LGG + Ga-poly (physical mixture of LGG and Ga-poly), and LGG@Ga-poly, followed by in situ

injection of Panc-02 cells into the pancreas (Fig. 5a). Three weeks later, mice were sacrificed and tumors were collected. The smallest tumor volume and the lightest tumor weight in the LGG@Ga-poly group indicated that LGG@Ga-poly could effectively delay tumorigenesis (Fig. 5b, c). The terminal deoxynucleotidyl transferase 2'-deoxyuridine, 5'-triphosphate (dUTP) nick end labeling (TUNEL) assay showed that LGG@Ga-poly induced the highest number of apoptotic tumor cells (Fig. 5d). Additionally, CD3-immunofluorescence staining of tumors indicated that LGG@Ga-poly potentiated antitumor T cell responses (Fig. 5e). The results obtained using the KPC mouse model also demonstrated that LGG@Ga-poly significantly inhibited the formation and growth of tumors (Supplementary Fig. 15a). Furthermore, when LGG@Ga-poly was administered orally to healthy mice over a three-month period, we observed no significant changes in immune-related indicators, indicating that long-term prevention with LGG@Ga-poly does not adversely affect the immune system (Supplementary Fig. 15b). Collectively, these findings suggest that LGG@Ga-poly significantly reduces PDA tumorigenesis, offering a potential preventative benefit for individuals at risk of pancreatic cancer.

We next evaluated the therapeutic efficacy of LGG@Ga-poly in a therapeutic setting. Orthotopic Panc-02-bearing mice were randomly divided into five groups, and all treatments were orally administered every two days for a total of eleven times (Fig. 5f). Real-time tumor growth was monitored using the IVIS system by measuring the bioluminescence of cancer cells. Mice treated with LGG@Ga-poly exhibited the weakest bioluminescence intensity, indicating the smallest tumor size (Supplementary Fig. 16a). Tumor growth was also monitored using magnetic resonance imaging (MRI) and μ -computerized tomography (μ -CT) imaging, where mice in the PBS-treated group showed obvious suspected areas, while almost no tumors were observed after LGG@Ga-poly treatment (Fig. 5g, h). The observation of resected tumors and tumor weighing also indicated the superior therapeutic efficacy of LGG@Ga-poly (Fig. 5i, j). Additionally, LGG@Ga-poly treatment induced the largest tumor necrosis regions and tumor cell apoptosis, as demonstrated by H&E and TUNEL staining, and significantly inhibited tumor cell proliferation, as shown by Ki67 staining (Fig. 5k). Bacterial Gram staining of tumors demonstrated that LGG@Ga-poly remarkably reduced the overall loads of LPS-expressing Gram-negative microbes, and Masson staining showed that LGG@Ga-poly-treated tumors had the least ECM deposition (Supplementary Figs. 16b, c). Furthermore, orally administered LGG@Ga-poly remarkably inhibited the lung metastasis of PDA tumors (Fig. 5l).

The safety profiles after LGG@Ga-poly treatment were then carefully evaluated in vivo. As all components used in the system, including LGG, chitosan, Ga³⁺, and EGCG, are classified as Generally Recognized as Safe (GRAS) and widely employed in medical practices, LGG@Ga-poly exhibited excellent biocompatibility and clinical translatability. Throughout the entire treatment period, there were only minor fluctuations in the body weight of mice, indicating no significant toxicity (Fig. 5m). H&E staining of major organs showed no visible abnormalities induced by LGG@Ga-poly. Blood biochemistry and blood routine tests further indicated the biosafety of LGG@Ga-poly treatment (Supplementary Fig. 17a, b).

We also investigated cancer stem cells across various treatment groups and found that the material treatments did not alter the proportion of cancer stem cells. Importantly, the percentage of cancer stem cells in the tumor mass of the LGG@Ga-poly-treated group was similar to that observed in the PBS-treated mice (Supplementary Figs. 17c–e). Additionally, we evaluated the antitumor efficacy of LGG@Ga-poly in the KPC mouse model. Six-week-old KPC mice were orally administered each material every two days for a total of twenty doses. After treatment, the mice were sacrificed, and the tumors were weighed. The results showed that LGG@Ga-poly treatment achieved the highest therapeutic efficacy (Supplementary Fig. 18).

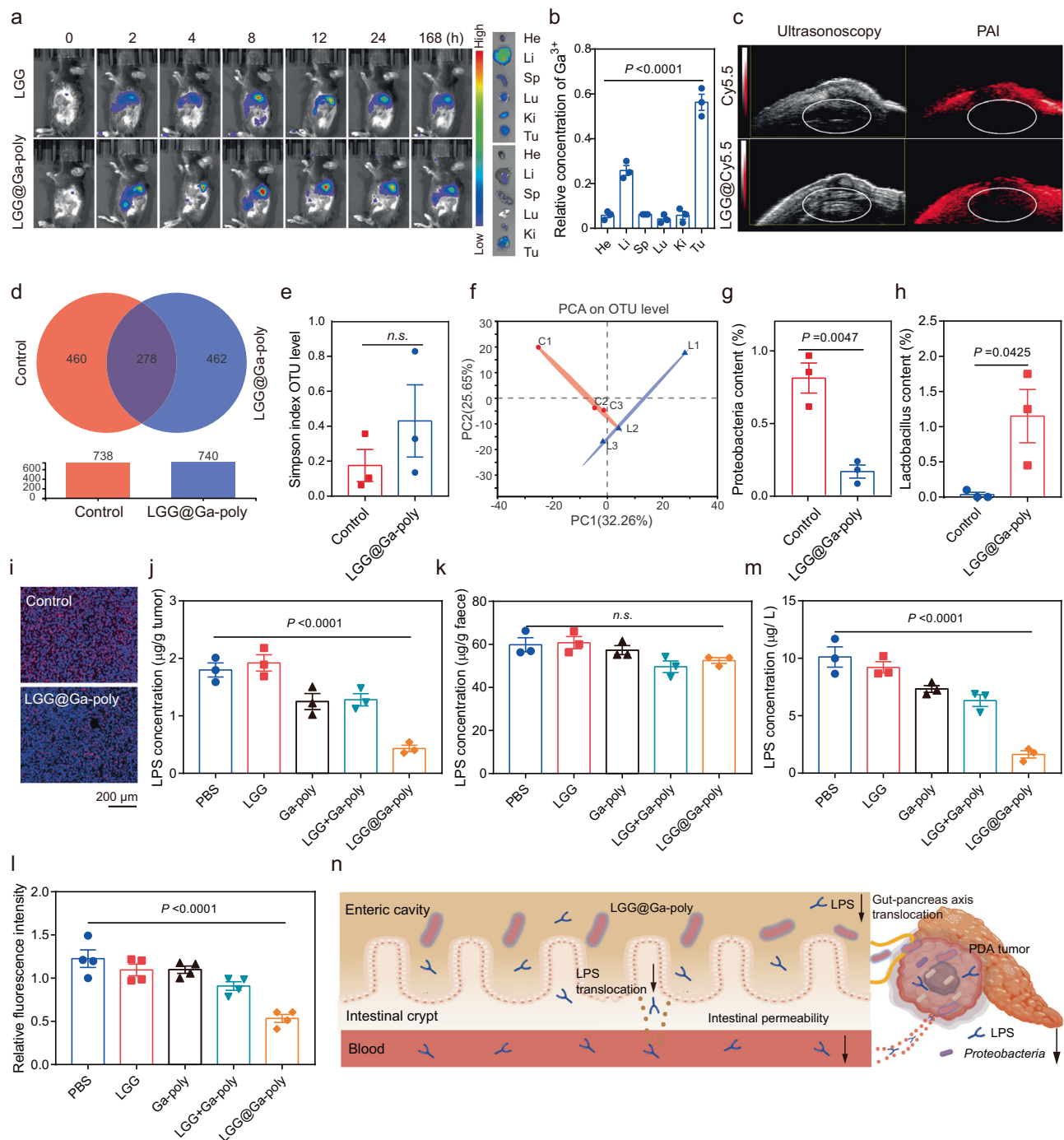


Fig. 4 | Modulation of intratumor microbiota by LGG@Ga-poly. **a** In vivo and ex vivo fluorescence imaging of orthotopic PDAC mice after oral administration of Cy5.5 labeled LGG or LGG@Ga-poly ($n = 3$ mice). **b** Relative concentration of Ga^{3+} within major organs and tumors after treatment with LGG@Ga-poly ($n = 3$ samples). He-heart, Li-liver, Sp-spleen, Lu-lung, Ki-kidney, Tu-tumor. **c** Ultrasonography and Photoacoustic (PAI) imaging of tumor areas treated with Cy5.5 or Cy5.5 labeled LGG@Ga-poly. Experiments were performed three times with similar results ($n = 3$ mice). **d** Venn diagram illustrating the strains of identified bacteria within tumor tissues in the control group and the LGG@Ga-poly treatment group ($n = 3$ samples). **e** The α -diversity of intratumor microbiota community (Simpson) in the control and LGG@Ga-poly treatment group ($n = 3$ samples). **f** Principal component analysis (PCA) analysis illustrating the β -diversity of intratumor microbiome in the control and LGG@Ga-poly treatment group ($n = 3$ samples; Control: C1–C3, LGG@Ga-poly: L1–L3). Contents of

intratumor **g** *Proteobacteria* and **h** *Lactobacillus* in the control and LGG@Ga-poly treatment group ($n = 3$ samples). **i** Bacterial loads within tumors with or without LGG@Ga-poly treatment, demonstrated by FISH staining. Experiments were performed three times ($n = 3$ mice). Concentration of LPS in the **j** tumor and **k** feces after different treatments ($n = 3$ samples). **l** Relative FITC fluorescence in the blood after different treatments ($n = 4$ samples). **m** Concentration of LPS in the blood in each group ($n = 3$ samples). **n** Schematic diagram illustrating that LGG@Ga-poly restores intestinal homeostasis and eliminates PDA tumor-promoting *Proteobacteria* as well as LPS. Significance between the two groups was calculated using two-tailed Student's *t*-tests (**e**, **g**, and **h**) or one-way ANOVA with Tukey post hoc test (**b**, **j**, **k**, **l**, and **m**). Data are means \pm sem. *n.s.* means no significance. Source data are provided as a Source Data file. Figure 4n, created with BioRender.com, was released under a Creative Commons Attribution-NonCommercial-NoDerivs 4.0 International license.

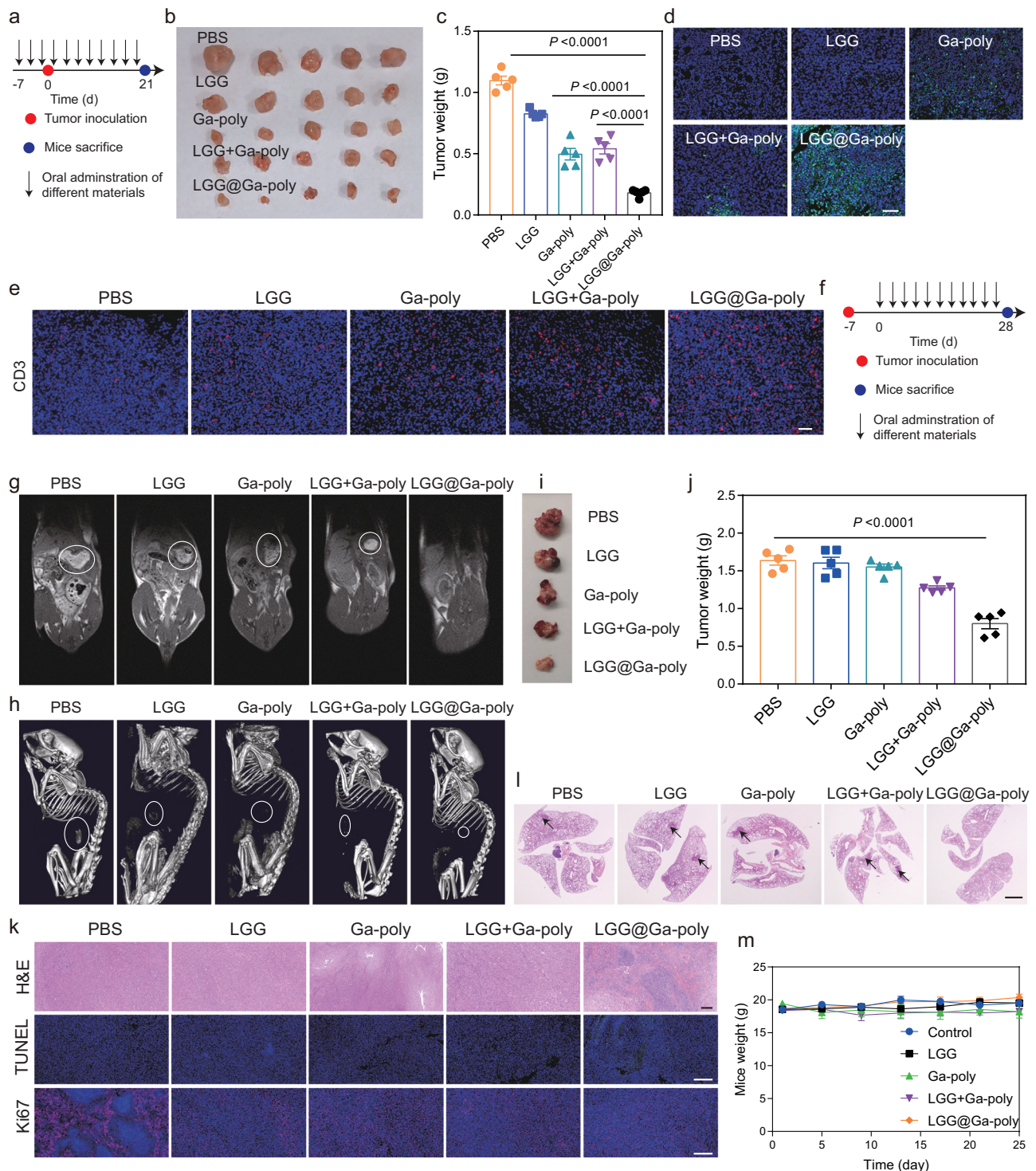


Fig. 5 | In vivo antitumor efficacy. Therapeutic efficacy in a prophylactic setting (**a–e**). **a** Prophylactic treatment regimen. **b** Photographs of tumors in each group ($n = 5$ mice). **c** Tumor weight in each group ($n = 5$ mice). **d** TUNEL staining of tumors after different treatments. The scale bar is 200 μ m. Experiments were repeated three times. $n = 5$ mice in each group. **e** CD3-immunofluorescence staining of tumor tissues after different treatments. The scale bar is 50 μ m. Experiments were repeated three times. $n = 5$ mice in each group. Therapeutic efficacy in a therapeutic setting (**f–l**). **f** Treatment scheme on established PDAC mice. Representative **g** magnetic resonance imaging (MRI) images and **h** computerized tomography (CT) images of PDAC mice after different treatments ($n = 5$ mice). The circles represent

suspicious tumor areas. Experiments were repeated three times. **i** Representative photographs of resected tumors in each group. $n = 5$ mice in each group. **j** Tumor weight in each group ($n = 5$ mice). **k** H&E, TUNEL, and Ki67 staining of tumor tissues after different treatments. The scale bars are 200 μ m. Experiments were repeated three times. $n = 5$ mice in each group. **l** H&E staining of lungs in each group. The scale bar is 1.5 mm. The arrows indicate metastatic tumor niches. Experiments were repeated three times. $n = 5$ mice in each group. **m** Body weight of mice after various treatments ($n = 5$ mice). Significance between two groups was calculated using one-way ANOVA with Tukey post hoc test (c and j). Data are means \pm sem. Source data are provided as a Source Data file.

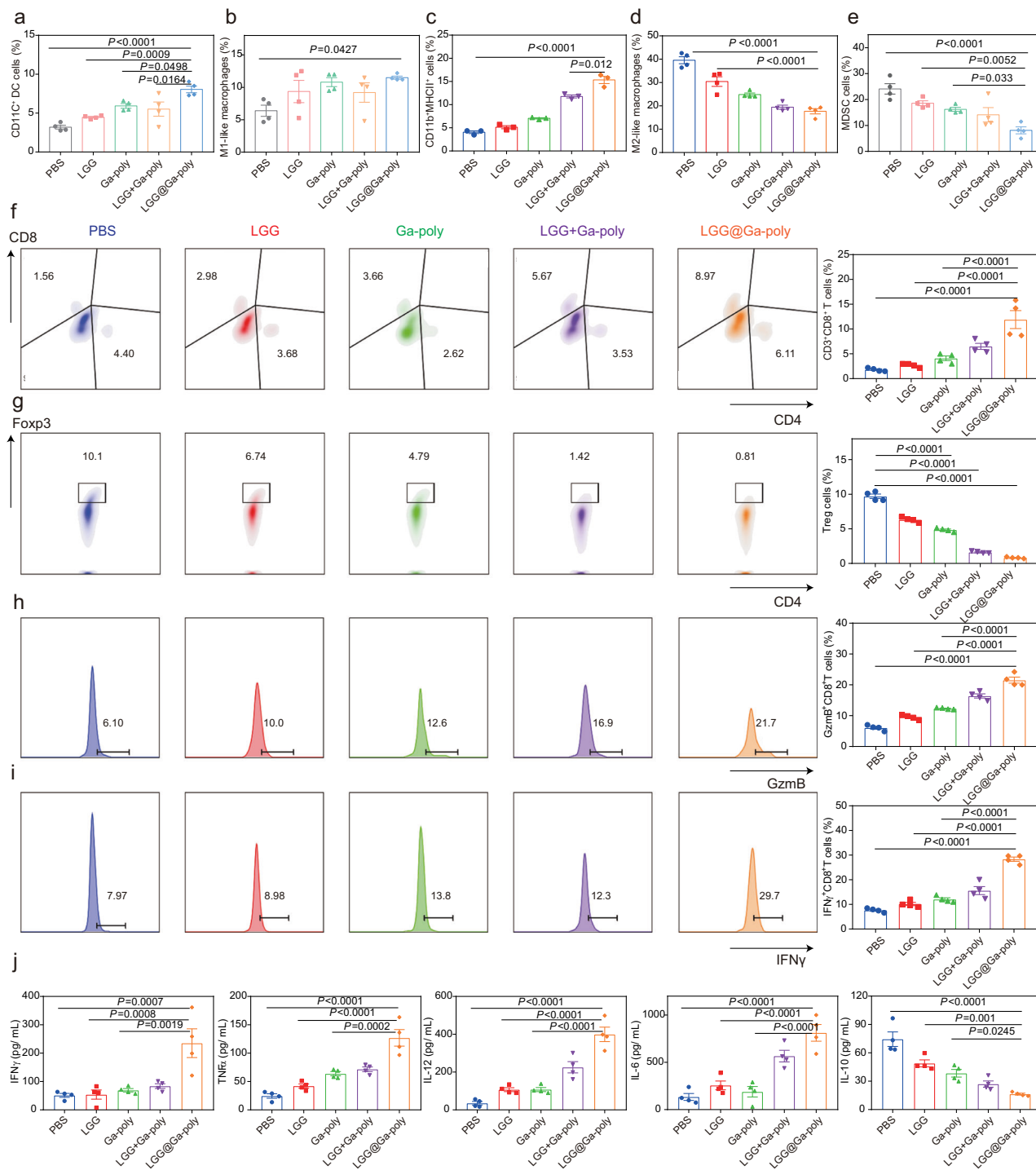


Fig. 6 | LGG@Ga-poly treatment induced an immune-active PDA TME. FCM analyzes of **a** CD11c⁺CD80⁺CD86⁺ DC cells in the lymph node ($n = 4$ samples), **b** CD11b⁺CD86⁺ M1-like macrophages in the tumor ($n = 4$ samples), **c** CD11b⁺MHCII⁺ cells in the tumor ($n = 3$ samples), **d** CD11b⁺CD206⁺ M2-like macrophages in the tumor ($n = 4$ samples) and **e** CD11b⁺CyL6⁺ MDSC cells in the tumor ($n = 4$ samples) after different treatments. FCM images and quantitative analysis of **f** CD3⁺CD8⁺ T cells in the tumor ($n = 4$ samples), **g** Foxp3⁺CD4⁺ Tregs in the tumor

($n = 4$ samples), **h** GzmB⁺CD8⁺ T cells in the tumor ($n = 4$ samples) and **i** IFN- γ ⁺CD8⁺ T cells in the tumor ($n = 4$ samples) after different treatments. **j** ELISA detections indicated the concentrations of intratumor cytokines after different treatments ($n = 4$ samples). Significance between two groups was calculated using one-way ANOVA with Tukey post hoc test. Data are means \pm sem. Source data are provided as a Source Data file.

Interplay between microbiota modulation and systemic anti-tumor immune responses

To investigate the impact of microbiota elimination on the immune TME, we assessed immune cell infiltration using FCM after administering various treatments. The results in Supplementary Fig. 19 showed

that after LGG@Ga-poly treatment, there was a significant increase in the proportion of APCs, including mature DCs and M1-like macrophages (Fig. 6a, b). The expression of MHCII on monocytes was also increased (Fig. 6c). In contrast, the number of M2-like macrophages and MDSCs associated with tumor immunosuppression was

significantly decreased following LGG@Ga-poly treatment (Fig. 6d, e). Furthermore, LGG@Ga-poly treatment led to the highest infiltration of CD8⁺ T cells within tumor tissues and significantly reduced the presence of immunosuppressive regulatory T cells (Tregs) (Fig. 6f, g). To further evaluate the functional changes in these CD8⁺ T cells, we detected the percentage of CD8⁺ T cells that secreted IFN- γ and granzyme B (Gzmb). Remarkably, the levels of both IFN- γ and Gzmb-positive CD8⁺ T cells were substantially increased following treatment with LGG@Ga-poly (Fig. 6h, i). Additionally, the LGG@Ga-poly-treated group exhibited a significant increase in effector memory T (T_{EM}) cells in the spleen compared to other groups (Supplementary Fig. 20a). Notably, PD-L1 expression by tumor tissues also significantly decreased after LGG@Ga-poly treatment (Supplementary Fig. 20b). A comprehensive analysis of immune-related cytokines within tumor tissues revealed that LGG@Ga-poly treatment led to a significant upregulation of antitumor cytokines, including IL-6, IL-12, IFN- γ , and TNF α , and a marked downregulation of immunosuppressive cytokines, such as IL-10 and IL-1 β , as shown in Fig. 6j and Supplementary Fig. 20c. These findings suggest LGG@Ga-poly effectively modulates the immune TME to promote an anti-tumor immune response.

To further assess the immune response within tumor tissues following treatment with LGG@Ga-poly, we conducted a transcriptomic analysis of 14,518 genes within the tumors. A Venn diagram was used to illustrate the gene expression relationship between the control and LGG@Ga-poly treatment group. Using a threshold of fold change ≥ 2 and $p < 0.05$, 1265 differentially expressed genes were identified (Fig. 7a), and a volcano plot was used to illustrate the differences in gene expression between the two groups (Fig. 7b). Genes associated with antitumor immunity were further analyzed by gene ontology (GO) function enrichment analysis, which demonstrated a significant enrichment in “regulation of innate immune response”, “positive regulation of immune effector process”, and “positive regulation of lymphocyte activation” after LGG@Ga-poly treatment (Fig. 7c). Kyoto encyclopedia of genes and genomes (KEGG) enrichment analysis revealed that the immune response activated by LGG@Ga-poly primarily relied on the “Toll-like receptor (TLR) signaling pathway”, “NOD-like receptor signaling pathway”, and “NF-kappa B signaling pathway” (Fig. 7d). These above results demonstrate that the innate immunity, especially the TLR signaling pathway is of significance on immune-activation by LGG@Ga-poly.

Following this, a comprehensive approach involving database analysis, in vitro assays, and in vivo experiments was undertaken to validate the capacity of LGG@Ga-poly to counteract PDA immunosuppression through the modulation of the LPS/TLRs signaling pathway. Our analysis of the TCGA database unveiled a substantial increase in the expression levels of TLRs in PDA tumors when compared to healthy pancreatic tissues (Fig. 7e, and Supplementary Fig. 21a)⁴³. Notably, the expression of TLR4 exhibited an inverse correlation with patient survival in pancreatic cancer, underscoring its potential adverse impact on patient outcomes (Supplementary Fig. 21b). Furthermore, a positive association was observed between TLR4 expression and CD274 (PD-L1) expression, suggesting the conceivable presence of an immunosuppressive effect linked to TLR4 activation (Supplementary Fig. 21c). Subsequent investigations encompassed an in vitro assay aimed at elucidating the impact of LPS stimulation on TLR4 expressed by macrophages. The short-term stimulation of LPS prompted the polarization of RAW264.7 macrophages towards the M1 phenotype; however, prolonged exposure to LPS for over 72 hours significantly elevated the proportion of immunologically tolerant M2-like macrophages (Fig. 7f, and Supplementary Fig. 21d, e). These findings indicate that extended LPS exposure within PDA tumors can instigate an immunosuppressive TME. Complementing this with in vivo evidence, we observed a significant reduction in TLR expression within tumor tissues upon LGG@Ga-poly treatment. Besides, when combined with LPS injection to sustain TLR/NF-kappa B signaling

activation, the immune-activating effect of LGG@Ga-poly was notably curtailed (Fig. 7g, h, and Supplementary Fig. 22). Correspondingly, discernible inhibition of tumor growth was not observed (Fig. 7i). Collectively, our findings elucidate that LGG@Ga-poly treatment effectively abrogates PDA immunosuppression by inhibiting microbial-dependent TLR activation within the TME.

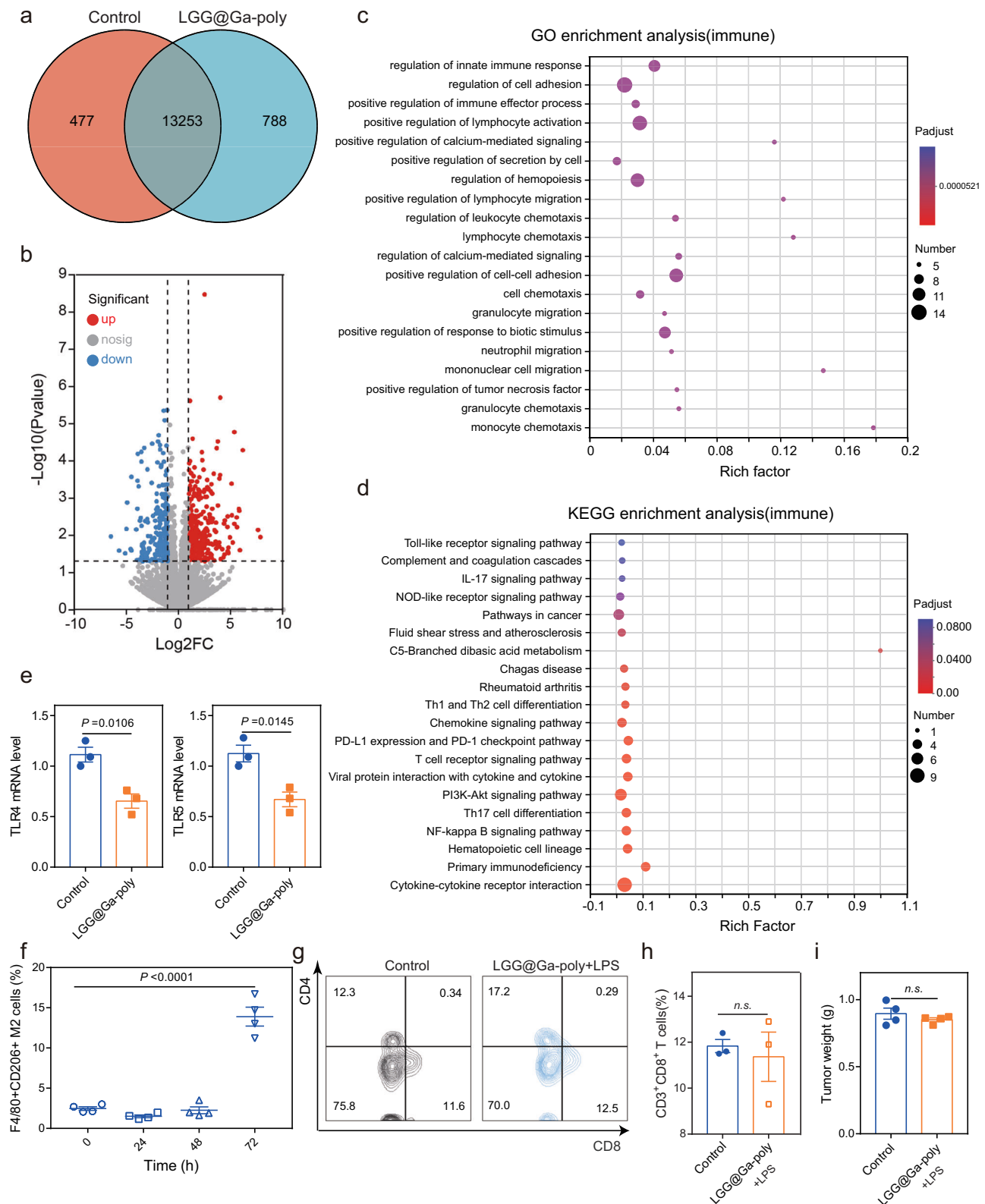
Synergistic effect with chemotherapy and immunotherapy

Finally, we evaluated the synergistic effect of LGG@Ga-poly treatment with gemcitabine (Gem) chemotherapy and ICB immunotherapy. Previous studies have shown that modulating the intratumor microbiota can enhance the efficacy of chemotherapy in PDAC^{44,45}. To assess the enhanced therapeutic effect of LGG@Ga-poly, we randomly assigned Panc-02-bearing mice into four groups: PBS, Gem, LGG@Ga-poly, and LGG@Ga-poly + Gem. LGG@Ga-poly was administered orally, while Gem was injected intravenously (Fig. 8a). Throughout the treatment period, the body weight of mice treated with LGG@Ga-poly + Gem fluctuated slightly, while Gem treatment alone led to a noticeable decline in mice weight, suggesting that the combination of Gem with LGG@Ga-poly could alleviate chemotherapy side effects (Fig. 8b). At the end of the treatment, mice were sacrificed, and tumors were dissected for weighing, which revealed that the combined therapy effectively suppressed tumor growth by approximately 80% compared to the PBS control, while Gem alone only inhibited tumor growth by about 15% (Fig. 8c). H&E staining and TUNEL assay indicated that LGG@Ga-poly combined with Gem induced the highest amount of apoptotic tumor cells, while showed no obvious toxicity on normal organs (Fig. 8d and Supplementary Fig. 23a). Immunofluorescence staining for CD3 demonstrated that LGG@Ga-poly plus Gem treatment potentiated T cell infiltration to the maximum extent possible (Fig. 8e). Blood biochemical and blood routine tests confirmed the in vivo safety of combination chemotherapy (Supplementary Fig. 23b). The level of the probiotic *Butyrivibrio* in the gut microbiome improved following treatment with LGG@Ga-poly plus chemotherapy, compared to the free Gem group. This suggests that LGG@Ga-poly plays a role in stabilizing the gut microbiome (Supplementary Fig. 23c).

Furthermore, we confirmed that LGG@Ga-poly treatment could enhance the therapeutic efficacy of α -PD-L1 immunotherapy. The therapeutic regimen is shown in Fig. 8f. The combination of LGG@Ga-poly and α -PD-L1 mostly inhibited tumor growth (Fig. 8g, h). Importantly, mice treated with the combined therapy survived beyond 60 days, while those treated with free α -PD-L1 all died within 45 days (Fig. 8i). Mice weight in each group was slightly changed (Fig. 8j). Additionally, we observed improved intratumor infiltration of CD8⁺ T cells with the combined LGG@Ga-poly and α -PD-L1 therapy (Fig. 8k). Moreover, H&E staining of normal organs indicated that the combined ICB therapy did not induce metastasis niches (Supplementary Fig. 24). These results indicate that LGG@Ga-poly has the potential to improve the effectiveness of PDAC treatment by further combining chemotherapy and ICB-based immunotherapy.

Discussion

This study highlights the crucial role of intratumor microbiota, specifically microbiota-derived LPS, in promoting immunosuppression and resistance to ICB treatment in PDAC. To address this, we have developed a biohybrid system called LGG@Ga-poly as an oral biotherapeutic for enhancing PDAC immunotherapy by modulating the microbiota-immune interactions. Orally administered LGG@Ga-poly selectively targets PDA tumors via gut-pancreas translocation and effectively eliminates intratumor microbiota and LPS via the biological competition of LGG and Ga³⁺-mediated microbial inactivation. This process disrupts the immunosuppressive TME by reducing TAMs and MDSCs, while increasing cytotoxic CD8⁺ T cells. The immune-activation mechanism is attributed to the inhibition of microbial-dependent activation of the TLR4/NF-kappa B signaling pathway. Moreover, LGG@Ga-poly



significantly delays PDA tumorigenesis in a preventive setting, and inhibits established tumor growth and lung metastasis, and enhances the efficacy of ICB immunotherapy. These findings provide evidence that biomaterials can be rationally designed to modulate intratumor microbiota for improving PDAC immunotherapy.

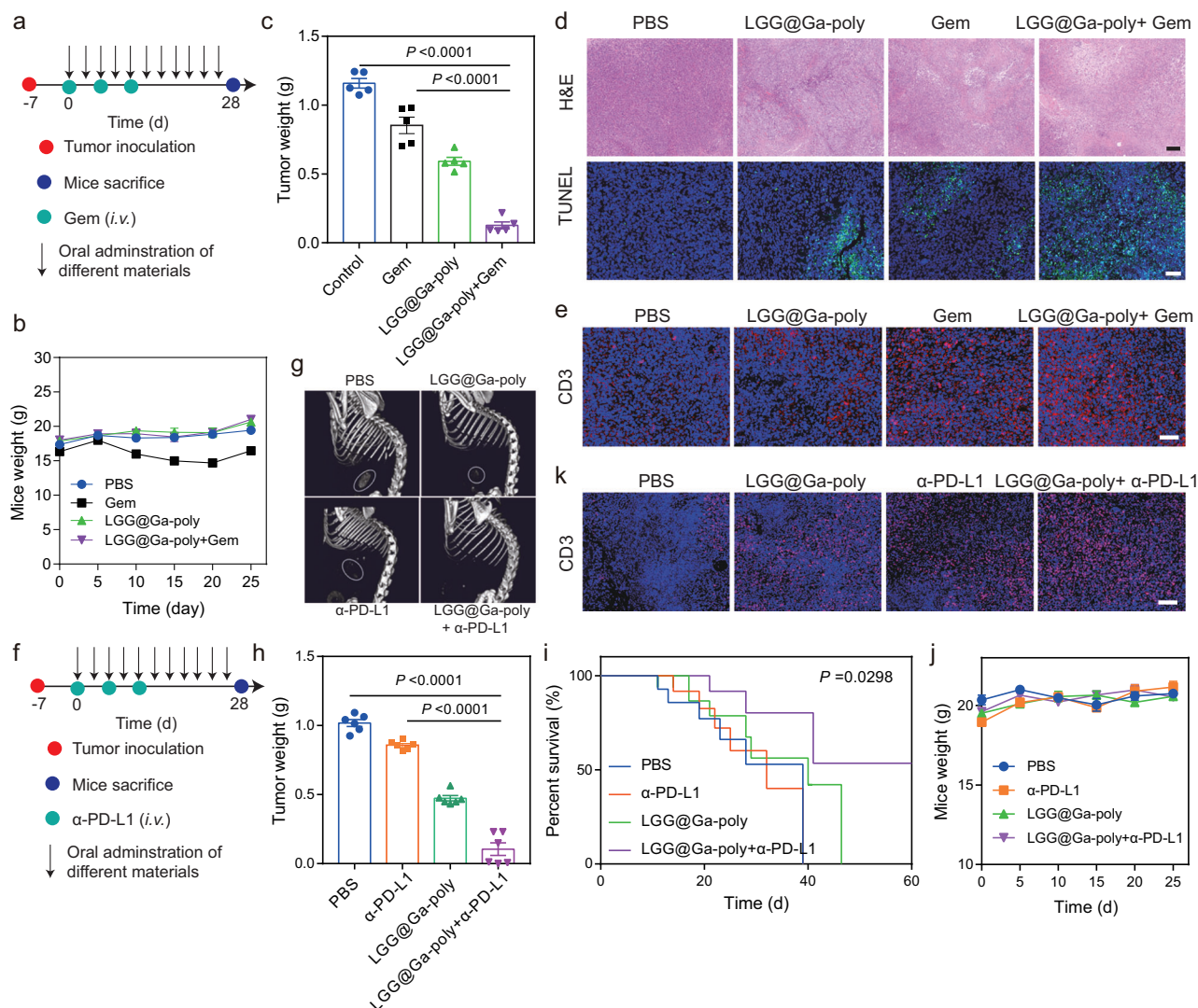
Our design offers several notable advantages. Firstly, the bactericidal action induced by Ga^{3+} relies on iron availability, which is not

required by LGG, ensuring that Ga^{3+} has no adverse effect on LGG viability. This characteristic makes LGG@Ga-poly highly stable and bioactive. Additionally, the exceptional tumor-targeting capability, coupled with chitosan protection, prevents premature release of free Ga^{3+} in the gastrointestinal tract, minimizing disruptions to gut microbiota equilibrium. Furthermore, all components of LGG@Ga-poly are GRAS, demonstrating excellent biocompatibility and

Fig. 7 | Mechanism analysis of LGG@Ga-poly for PDA immune activation.

Transcriptomic analysis (a–d). **a** Venn diagram of primary transcripts of PDA tumors in the control group and the LGG@Ga-poly treatment group ($n = 4$ samples). **b** Volcano plot for identifying differentially expressed genes with and without LGG@Ga-poly treatment ($n = 4$ samples). Differential expression genes were determined using the DESeq2R package. The P-values were adjusted using the Benjamini and Hochberg's approach for controlling the false discovery rate, $P_{\text{adj}} \leq 0.05$ and $|\log_2(\text{foldchange})| \geq 1.0$ were set as the thresholds for significant differential expression. **c** GO enrichment analysis of major types of immune-related biological processes after LGG@Ga-poly treatment, and the top 20 terms were selected ($n = 4$ samples). **d** KEGG pathway analysis of immune-related genes of PDA tumors treated with LGG@Ga-poly, and the top 20 terms were selected

($n = 4$ samples). Statistical significance was assessed using a two-sided hypergeometric test, with p-values adjusted for multiple comparisons using the Benjamini-Hochberg method (c, d). **e** Changes of TLR4 and TLR5 mRNA levels in PDA tumors after LGG@Ga-poly treatment ($n = 3$ samples). **f** In vitro analysis of polarization of RAW264.7 cells into M2 type after LPS treatment for different time points ($n = 4$ samples). **g** FCM images and **h** quantitative analysis of CD3⁺CD8⁺ T cells in PDA tumors in the control group and the LGG@Ga-poly + LPS treatment group ($n = 3$ samples). **i** Tumor weight in the control group and the LGG@Ga-poly + LPS treatment group ($n = 4$ mice). Significance between two groups was calculated using two-tailed Student's t-tests (e, h, and i) or one-way ANOVA with Tukey post hoc test (f). Data are means \pm sem. n.s. means no significance. Source data are provided as a Source Data file.

**Fig. 8 | Synergistic antitumor effect with chemotherapy and α -PD-L1 therapy.**

Combined LGG@Ga-poly with chemotherapy (a–e). **a** Treatment route of combined LGG@Ga-poly with chemotherapy. **b** Mice weight treated by PBS, Gem, LGG@Ga-poly, and LGG@Ga-poly + Gem ($n = 5$ mice). **c** Tumor weight after different treatments ($n = 5$ mice). **d** H&E and TUNEL and **e** CD3-immunofluorescence staining of tumors after different treatments. The scale bars are 50 μm . Experiments were repeated three times. $n = 5$ mice in each group. Combined LGG@Ga-poly with ICB immunotherapy (f–j). **f** Treatment route of combined LGG@Ga-poly with α -PD-L1 therapy. **g** μ -CT imaging of PDA tumor-bearing mice treated by PBS, α -

PD-L1, LGG@Ga-poly, and LGG@Ga-poly + α -PD-L1. The circles represent abnormal areas. Experiments were repeated three times. $n = 6$ mice in each group. **h** Tumor weight after different treatments ($n = 6$ mice). **i** Survival curves of mice after different treatments ($n = 6$ mice). **j** Mice weight after different treatments ($n = 6$ mice). **k** CD3-immunofluorescence staining of tumors after different treatments. The scale bar is 50 μm . Experiments were repeated three times. $n = 6$ mice in each group. Significance between two groups was calculated using one-way ANOVA with Tukey post hoc test (c, h, and i). Data are means \pm sem. Source data are provided as a Source Data file.

potential for clinical translation. In conclusion, this research paves the way for the development of highly targeted living materials that can modulate the tumor microbiome, thereby enhancing the effectiveness of cancer immunotherapy for various types of microbe-colonized cancer.

Methods

This research complies with all relevant ethical regulations approved by the Institutional Animal Care and Use Committee (IACUC) of the Animal Experiment Center at Wuhan University, China. All mice were housed at 12-h light-dark cycle within 25–27 °C and 45–55% humidity. In our work, no subcutaneous tumor burden exceeds 2000 mm³, which meets the maximum tumor burden permitted by the protocol of the Animal Care and Use Committee of Wuhan University. Tumor volume was calculated as: width²×length/2. For orthotopic tumor-bearing mice, mice were euthanized when the animals became moribund, exhibiting severe weight loss, extreme weakness, or unhealing ulceration. All experimental mice were female. The study design did not account for gender differences, given their minimal impact on the influence of intratumor microbiota on pancreatic cancer.

Materials

Ga(NO₃)₃·6H₂O (CAS: 69365-72-6), tannin (TA, CAS: 1401-55-4), gallic acid (GA, CAS: 149-91-7), epigallocatechin gallate (EGCG, CAS: 989-51-5), and chitosan (CS, CAS: 9012-76-4) were purchased from Sino-pharm Group Co. Ltd. Cyanine 5.5 (Cy5.5, CAS: 146368-15-2) was purchased from Beyotime Institute of Biotechnology. FITC-dextran (CAS: 60842-46-8) and LPS (CAS: 297-473-0) were purchased from Shanghai Aladdin Biochemical Technology Co., Ltd. Luria-Bertani (LB) medium, M9 liquid medium, Brain-Heart Infusion Broth (BHI) medium, and MRS Broth medium were purchased from Guangdong Huankai Microbial SCI & Tech Co., Ltd. Cell culture dishes/plates and 20-mm glass-bottom dishes were purchased from NEST Biotechnology co., Ltd. Dulbecco's Modified Eagle Medium (DMEM) was acquired from Sperikon Life Science & Biotechnology co., Ltd. Fetal bovine serum (FBS), penicillin, streptomycin, and trypsin were obtained from VivaCell (Shanghai, China). Transwell chamber was purchased from Zhejiang Saining Biotechnology Co., Ltd. Dimethyl-thiazol-2-yl]-2,5-diphenyltetrazoliumbromide (MTT), were obtained from GIBCO Invitrogen Corp.

Antibodies

The antibodies used for FCM were as follows: anti-mouse CD3 (FITC, Catalog number: 100203, Clone: 17A2, 1:50 dilution), anti-mouse CD4 (APC, Catalog number: 100411, Clone: GK1.5, 1:100 dilution), anti-mouse CD8a (PE, Catalog number: 100707, Clone: 53-6.7, 1:100 dilution), anti-mouse CD11c (FITC, Catalog number: 117305, Clone: N418, 1:200 dilution), anti-mouse CD80 (PE, Catalog number: 104707, Clone: 16-10A1, 1:50 dilution), anti-mouse CD86 (APC, Catalog number: 105011, Clone: GL1, 1:100 dilution), anti-mouse CD11b (APC, Catalog number: 101211, Clone: M1/70, 1:100 dilution), anti-mouse Ly-6G (Gr-1) (FITC, Catalog number: 108405, Clone: RB6-8C5, 1:200 dilution), anti-mouse F4/80 (FITC, Catalog number: 123107, Clone: BM8, 1:200 dilution), anti-mouse CD206 (PE, Catalog number: 141705, Clone: C068C2, 1:50 dilution), anti-mouse CD44 (PE, Catalog number: 103023, Clone: IM7, 1:100 dilution), anti-mouse CD62L (APC, Catalog number: 104411, Clone: MEL-14, 1:100 dilution), anti-mouse CD4 (PE, Catalog number: 116006, Clone: RM4-4, 1:100 dilution), anti-mouse CD8a (APC, Catalog number: 100711, Clone: 53-6.7, 1:100 dilution), anti-mouse Foxp3 (PE, Catalog number: 126403, Clone: MF-14, 1:20 dilution), anti-mouse IFN γ (PE, Catalog number: 163503, Clone: W18272D, 1:200 dilution), anti-mouse GzmB (PE, Catalog number: 372207, Clone: QA16A02, 1:20 dilution). All antibodies used for FCM and anti-PD-L1 antibody were purchased from BioLegend.

Characterization

SEM images were obtained on Zeiss Sigma FESEM. TEM images were obtained by a JEM-2100 (JEOL) transmission electron microscope. Zeta potential was measured on a Nano-ZS ZEN3600 particle sizer (Malvern Instruments). UV-vis absorbance was measured by UV-vis spectroscopy (Lambda Bio40). Confocal microscopy images were obtained from a confocal laser scanning microscope (CLSM, Nikon CI-si TE2000). Cell viability was evaluated through the MTT assay using a microplate reader (Bio-Rad, Model 550, USA). Blood routine was measured by an Auto Hematology Analyzer (MC-6200VET), and blood biochemistry was analyzed by a biochemical auto analyzer (MNCHIP, Tianjin, China). In vivo imaging was performed by a Spectrum Pre-clinical In vivo Imaging System (Pekin Emer). μ -CT scanning was conducted on a Quantum FX microCT system (PerkinElmer). MRI imaging was obtained from an Aspect M3 MRI imaging system (Israel). PAI imaging was conducted by a Vevo[®] LAZR system (visualSonics, Canada). Immune cell fluorescence intensity was analyzed by flow cytometry (BD FACS Aria III, USA).

Bacteria culture

E. coli and *S. aureus* were grown aerobically in LB medium consisting of 10 mg mL⁻¹ tryptone, 5 mg mL⁻¹ yeast extract, and 0.5 mg mL⁻¹ NaCl, overnight at 37 °C. *B. subtilis* was grown aerobically in BHI medium containing 17.5 mg mL⁻¹ brain heart immersion powder, 2 mg mL⁻¹ D-glucose, 10 mg mL⁻¹ tryptone, 5 mg mL⁻¹ NaCl, and 2.5 mg mL⁻¹ NaH₂PO₄, at 37 °C for 24 hours. *F. nucleatum* was anaerobically grown in BHI medium at 37 °C for 24 hours. LGG was anaerobically grown in Modified MRS medium consisting of 10 mg mL⁻¹ proteose peptone, 5 mg mL⁻¹ beef extract, 4 mg mL⁻¹ yeast extract, 20 mg mL⁻¹ dextrose, 1 mg mL⁻¹ polysorbate 80, 2 mg mL⁻¹ ammonium citrate, 5 mg mL⁻¹ sodium acetate, 2 mg mL⁻¹ dipotassium phosphate, 0.1 mg mL⁻¹ magnesium sulfate, and 0.05 mg mL⁻¹ manganese sulfate, at 37 °C for 24 hours. All bacterial lines were purchased from China Center for Type Culture Collection (CCTCC).

Cell culture

The human pancreatic cancer cell line Panc-01 (Catalog no. GDC0309), human pancreatic stellate cell line HPSC (Catalog no. GPC0058), and RAW264.7 (Catalog no. GDC0143) cell lines were obtained from CCTCC. The mouse pancreatic cancer cell line Panc-02 (CL-0736) were kindly provided by Wuhan Pricella Biotechnology Co., Ltd. Panc-02, Panc-01, and HPSC were cultured in a humidified atmosphere with 5% CO₂ using DMEM supplemented with 10% FBS (v/v) and 1% antibiotics (penicillin-streptomycin, 10,000 U mL⁻¹) at 37 °C. The Panc-02^{luc} cell line, which was transfected with luciferase, was cultured in DMEM containing 5% puromycin to maintain the selection pressure for the transfected cells. The RAW264.7 macrophage cell line was cultured in DMEM supplemented with heat-inactivated FBS. Panc-02 cell line was authenticated by short tandem repeat (STR) profiling, and other cell lines we used were morphologically confirmed according to the information provided by CCTCC.

Murine tumor models

Six-week-old C57BL/6 female mice (18 ± 2 g) were obtained from the Animal Biosafety Level III Lab at Wuhan University. All animal experimental procedures were conducted in accordance with the guidelines set by the Institutional Animal Care and Use Committee (IACUC) of the Animal Experiment Center at Wuhan University, China. To establish a subcutaneous PDAC mouse model, each mouse was injected with 100 μ L of Panc-02 cells (1 × 10⁶ cells per mouse) into the right flank. The mice were then monitored for 7 days to allow tumor development. For the establishment of an orthotopic PDAC mouse model, 50 μ L of luciferase-transfected Panc-02^{luc} cells (1 × 10⁶ cells per mouse) were inoculated into the pancreas of each mouse. After transplantation, the mice were observed for 7 days to allow tumor growth.

In vivo antitumor efficacy of α -PD-L1

The Panc-02-bearing mice were randomly assigned to two groups in subcutaneous or orthotopic tumor-bearing mouse models (nine mice in each group). The treatment group received intraperitoneal injections of 100 μ L of 0.6 mg kg⁻¹ α -PD-L1 on the 3rd, 6th, and 9th day, while the control group was treated with 100 μ L of PBS. Tumor volume was measured every other day for a total of eighteen days. In the orthotopic Panc-02-bearing mouse model, tumor volume was assessed by monitoring the bioluminescence of cancer cells using the IVIS system.

In vivo antitumor efficacy of antibiotics with α -PD-L1

Orthotopic Panc-02-bearing PDAC mice were randomly assigned to two groups (six mice in each group). One group was orally administered polymyxin B (50 mg kg⁻¹) on the 3rd, 6th, and 9th day, while the other group received 100 μ L of PBS. On the 3rd, 6th, and 9th day, both groups were intraperitoneally injected with 100 μ L of 0.6 mg kg⁻¹ α -PD-L1. Tumor progression was monitored and recorded using IVIS imaging, and histological analysis was performed to further assess the effects of the treatments on tumor growth. KPC mice, expressing mutant intrapancreatic Kras and Trp53, were obtained from Cyagen Biosciences Inc. (Suzhou, China). Six-week-old female mice were divided into two groups (five mice in each group). One group received oral administration of 100 μ L polymyxin B (50 mg kg⁻¹) combined with 0.6 mg kg⁻¹ α -PD-L1 weekly for six weeks. The control group was given 100 μ L of PBS with 0.6 mg kg⁻¹ α -PD-L1 on the same schedule. Post-treatment, the mice were sacrificed, and the tumors were resected and weighed.

In vitro effect of LPS

The cytotoxicity of LPS on Panc-02 cells was assessed using an MTT assay. Initially, Panc-02 cells were seeded at a density of 1×10^4 cells per well (100 μ L) in a 96-well plate and cultured for 24 hours. Different concentrations of LPS (100 μ L) were added to each well, followed by another 24-hour incubation. Subsequently, MTT solution (20 μ L, 5 mg mL⁻¹ in PBS) was added to each well, and the cells were incubated for an additional 4 hours. After removal of the culture medium, 150 μ L of DMSO was added to dissolve the formazan product. The absorbance at 570 nm was measured using a microplate reader. To evaluate the migration ability of the tumor cells, a cell scratch assay was performed. Panc-02 cells were seeded in a 6-well plate at a density of 5×10^4 cells per well and cultured for 24 hours. Sterile p200 pipette tips were used to create scratches on the plates, and the unattached tumor cells were removed by washing with sterile PBS. Subsequently, 1 mg L⁻¹ of LPS was added to the plates, and the attached cells were co-cultured for another 24 hours. The migration of Panc-02 cells was assessed by capturing photographs using inverted microscopes.

Effect of LPS on in vivo tumor growth and immune response

To investigate the impact of LPS on tumor development and immune response, C57BL/6 mice were transplanted with either 1×10^6 Panc-02^{luc} cells with 1 μ g g⁻¹ LPS or 1×10^6 Panc-02^{luc} cells without LPS in their pancreas (five mice in each group). After a period of four weeks, the mice were euthanized, and tumor tissues were collected for histological staining to examine cellular characteristics. Additionally, immune TME analysis was conducted to evaluate the immune response within the tumor tissues.

Screening antibacterial metal ions

To screen for the antibacterial activity of metal ions, four bacterial species (*E. coli*, *S. aureus*, *B. subtilis*, and LGG) were cultured individually for 24 hours. Each bacterial species was then co-cultured with eight different metal ions, each at a concentration of 50 μ g mL⁻¹, for 12 hours. After the incubation period, the growth of each bacterial species was measured by recording the OD600.

Antibacterial evaluation of Ga³⁺

To evaluate the antibacterial effectiveness of Ga³⁺ against *E. coli*, *B. subtilis*, and LGG, the bacteria were cultured in 10 mL of M9 medium with an initial inoculation dose of 0.1%. Ga(NO₃)₃·6H₂O solutions at a concentration of 50 μ g mL⁻¹ were added to the cultures. The OD600 of the cultures was measured after 12, 24, and 36 hours of co-culture to assess bacterial growth inhibition. In addition, *E. coli* was cultured in M9 medium and treated with Ga(NO₃)₃·6H₂O at a concentration of 50 μ g mL⁻¹. Combinations of Ga(NO₃)₃·6H₂O (50 μ g mL⁻¹) with TA (50 μ g mL⁻¹), EGCG (50 μ g mL⁻¹), or GA (50 μ g mL⁻¹) were also added to the *E. coli* culture, respectively. After 24 hours of co-culture, samples from each group were taken and plated onto agar to count bacterial colonies. To determine the uptake of Ga³⁺ by the bacterial cells, the Ga³⁺ concentration was measured using ICP analysis.

Preparation of LGG@Ga-poly

LGG@Ga-poly was prepared using a layer-by-layer self-assembly method. Initially, LGG was cultured in MRS medium for 24 hours and subsequently resuspended in PBS to achieve a concentration of 5×10^8 CFU mL⁻¹. Next, 10 mL of the LGG suspension was mixed with an equal volume of 5 mg mL⁻¹ chitosan solution and stirred gently for one hour. Following centrifugation at 2239 g for 5 minutes, the bacteria were dispersed in 49 mL of PBS. To prepare the LGG@Ga-EGCG complex, 500 μ L each of 40 mg mL⁻¹ EGCG and 10 mg mL⁻¹ Ga(NO₃)₃·6H₂O were rapidly added to the bacterial dispersion. The resulting solution was vigorously stirred for one hour, resulting in the formation of LGG@Ga-EGCG. Subsequently, 10 mL of a 5 mg mL⁻¹ chitosan solution was added to the LGG@Ga-EGCG mixture and stirred for an additional hour to obtain the final product, LGG@Ga-poly.

Environmental tolerance of LGG@Ga-poly

To evaluate the resistance of LGG@Ga-poly in the gastrointestinal (GI) environment, the following experimental procedure was conducted. Initially, a population of 5×10^8 CFU of LGG@Ga-poly was exposed to anaerobic conditions and treated with SGF and SCF at 37 °C for 24 hours. Subsequently, the bacteria were collected and cultured in MRS medium with an initial inoculation of 0.5%. After 24 hours of growth, 150 μ L of the culture medium was extracted, and the OD600 was measured as an indicator of bacterial growth.

Ga³⁺ release performance of LGG@Ga-poly

The concentration of Ga³⁺ was determined using ICP analysis, measuring both the initial concentration (C1) and the residual concentration (C2) after the self-assembly process. The loading efficiency (LE) of Ga³⁺ was calculated using the following formula: LE (%) = (C1 - C2) / C1 × 100%. To investigate the release behavior of Ga³⁺ from LGG@Ga-poly in SGF, 1 mL of a 5×10^8 CFU suspension of LGG@Ga-EGCG or LGG@Ga-poly was placed in dialysis bags with a molecular weight cut-off (MWCO) of 3000. These bags were then immersed in 9 mL of PBS (pH 2.0) and incubated at 37 °C on a shaker. After 4 hours, the dialysates were collected, and the concentration of Ga³⁺ was analyzed using ICP.

Antibacterial activity of LGG@Ga-poly

E. coli, *S. aureus*, and *F. nucleatum* were cultured in a 6-well plate for 24 hours. Subsequently, transwell chambers containing 1% LGG@Ga-poly at a concentration of 5×10^8 CFU were placed on the plate. After another 24 hours of co-culture, bacterial growth in the plate was quantified by measuring the OD600. Additionally, 100 μ L of bacterial solutions were extracted and spread on agar plates for 24 hours to observe bacterial colonies. To establish a *F. nucleatum*-infected Panc-02 cell model, Panc-02 cells were seeded in 6-well plates and cultured overnight. Then, the cells were incubated with *F. nucleatum* at mid-logarithmic phase (6×10^6 CFU) for 1 hour to allow for phagocytosis. After the extracellular bacteria were eliminated by treatment with metronidazole (MTD) (100 μ g mL⁻¹) for 2 hours, the bacteria-infected

cells were cultured at 37 °C for another 24 hours. Then, cells were treated with PBS, $\text{Ga}(\text{NO}_3)_3 \cdot 6\text{H}_2\text{O}$ ($50 \mu\text{g mL}^{-1}$) or LGG@Ga-poly (5×10^8 CFU) for another 24 hours. Afterwards, cells were washed with sterile PBS and lysed using 0.1% Triton X-100 in a 0.1% BSA aqueous solution for 2 hours. The resulting suspensions were diluted with PBS, and aliquots were plated for analysis.

Antibacterial activity within a bacteria-infected 3D tumor sphere

Panc-01 cells and HPSC cells were cultured as spheroids in a 96-well plate. Specifically, each well was supplemented with $50 \mu\text{L}$ of 1% agarose solution using microwave heating. Subsequently, Panc-01 cells were added at a density of 4000 cells per well and HPSC cells at a density of 2000 cells per well in $150 \mu\text{L}$ of agarose gel plate. After one week of growth, well-defined spheroids were observed, which were then replenished with fresh medium to establish 3D PDAC stroma-rich spheroids within another week. To assess the penetration ability, free Cy5 and Cy5-labeled LGG@Ga-poly with equivalent fluorescence intensity were incubated with the spheroids for 24 hours. After removing the medium, the fluorescence of Cy5 was visualized using CLSM at a magnification of $10\times$. Furthermore, to evaluate the antibacterial efficacy, Mcherry-expressing *E. coli* (1×10^8 CFU) were co-cultured with the spheroids for 24 hours. Subsequently, either free FITC or FITC-labeled LGG@Ga-poly was added. After an additional 24 hours of incubation, the fluorescence of FITC and Mcherry was visualized using CLSM. Moreover, free Ga^{3+} and LGG@Ga-poly containing an equivalent amount of Ga^{3+} (1 mg mL^{-1}) were incubated with *E. coli*-infected spheroids for 24 hours. The concentrations of Ga^{3+} and LPS within the spheroids were measured using ICP and an LPS detection kit, respectively.

In vivo biodistribution analysis

Orthotopic Panc-02 tumor-bearing mice were randomly divided into two groups, with three mice in each group. Subsequently, the mice were orally administered $100 \mu\text{L}$ of either 5×10^8 CFU Cy5.5-labeled LGG or Cy5.5-labeled LGG@Ga-poly. The whole-body fluorescence of the mice was monitored at predetermined time intervals using the IVIS system. Upon completion of the experiment, the mice were euthanized, and tumor tissues along with major organs were collected for ex vivo imaging analysis and histological staining. Furthermore, tumors and major organs from the LGG@Ga-poly-treated group were collected and homogenized to measure Ga^{3+} concentration. To evaluate the tumor-penetrating ability, photoacoustic imaging was conducted 12 hours after oral administration of Cy5.5 or Cy5.5-labeled LGG@Ga-poly.

Microbiota analysis

To compare the microbial communities in PDA tumors and healthy pancreases, an orthotopic Panc-02 tumor-bearing mice model was established. The tumors were allowed to progress for one month, after which PDA tumor tissues and a healthy pancreas were collected under sterile conditions. The microbiota present in these samples was analyzed using 16S rDNA sequencing, a technique commonly used for bacterial community profiling. To assess the impact of LGG@Ga-poly treatment on the intratumor microbiota, tumors were collected after six treatments for microbiota analysis. Additionally, fecal pellets were collected to analyze any changes in the gut microbiota.

In vivo intestinal permeability evaluation

In the in vivo evaluation of intestinal permeability, the potential protective effect of LGG@Ga-poly was investigated through an intestinal permeability assay using FITC-dextran as a marker. After completing the treatment regimen, mice were fasted for 4 hours to establish a consistent baseline condition. Subsequently, the mice were orally administered with 0.6 mg g^{-1} of 4 kDa FITC-dextran. After an additional

3 hours, peripheral blood samples were collected from the mice, and the fluorescence intensity of FITC in the serum samples was measured to evaluate the intestinal permeability. The fluorescence intensity served as an indicator of the extent of FITC-dextran crossing the intestinal barrier and entering the bloodstream, allowing for the assessment of intestinal permeability.

LPS measurement

Following the administration of different treatments, samples including whole blood, fecal pellets, and tumor tissues were collected and transferred into EP tubes. The blood samples were left to rest at room temperature for 1 hour and then subjected to centrifugation at 861 g for 10 minutes to separate the serum from other components. The obtained serum, along with the supernatants from the fecal and tumoral samples, was collected for measuring the concentration of LPS by a LPS detection kit.

In vivo therapeutic efficacy in a prophylactic setting

The mice were randomly divided into five groups: PBS, LGG, Ga-poly, LGG + Ga-poly, and LGG@Ga-poly (five mice in each group). Prior to tumor cell implantation (Day 0), the mice were administered $100 \mu\text{L}$ of the respective materials every other day for a total of three treatments (starting from Day -7). Subsequently, the mice received continued treatment every other day for a total of eight treatments. The doses of each material were as follows: LGG (5×10^8 CFU), Ga-poly (5 mg kg^{-1}), LGG + Ga-poly (5×10^8 CFU LGG + 5 mg kg^{-1} Ga-poly), and LGG@Ga-poly (5×10^8 CFU). On Day 21, the mice were sacrificed, and the tumors were visually inspected and weighed. The T cell infiltration in the tumors was quantified using CD3-immunofluorescence staining. Additionally, six-week-old female KPC mice were divided into two groups (five mice in each group). One group was orally administered LGG@Ga-poly (5×10^8 CFU) every other day, totaling twenty treatments. The control group received $100 \mu\text{L}$ of PBS on the same schedule. After the treatment period, the mice were sacrificed, and their tumors were resected and weighed.

In vivo antitumor efficacy of LGG@Ga-poly

Mice with Panc-02 tumors were randomly divided into five groups: PBS, LGG, Ga-poly, LGG + Ga-poly, and LGG@Ga-poly (five mice in each group). Starting from Day 0, the mice received various treatments every other day for a total of eleven times, with the same doses as in the prophylactic setting. The tumor volume was monitored using IVIS, MRI, and CT imaging techniques. On Day 28, the mice were sacrificed for ex vivo histological analysis. Furthermore, six-week-old female KPC mice were organized into five groups, each comprising five mice. They underwent various treatments every other day, totaling twenty sessions, with dosages consistent with those used in the prophylactic setting for the Panc-02 model. Following the treatment period, the mice were euthanized, and their tumors were excised and weighed.

Immune TME analysis

The immune cells present in tumor tissues, lymph nodes, and spleen were analyzed quantitatively using flow cytometry after staining. Specifically, the tumor tissues were processed into single-cell suspensions using collagenase IV (Roche), DNAase I (BioFroxx), and hyaluronidase (bioSharp) at 37 °C for 2 hours. The resulting cell suspension was subjected to red blood cell lysis and dispersed in PBS (1 mL). The cell suspension was then filtered through a $70 \mu\text{m}$ cell strainer and separated using percoll (Stem Cell). The single-cell suspensions were subsequently stained with antibody cocktails, and fluorescently labeled cells were counted using a BD Accuri™ C6 flow cytometer. The immune cell populations that were analyzed included M1-like and M2-like macrophages, MDSCs, DCs, T cells, and memory effector T (T_{EM}) cells.

Transcriptome analysis

Tumor samples from both the PBS treated group ($n=3$) and the LGG@Ga-poly group ($n=3$) were excised and promptly preserved at -80°C before further processing. Total RNA was extracted from the tumor samples by using TRIzol Reagent (Invitrogen), and the genomic DNA was eliminated through DNase I treatment (TaKara). The RNA samples were then assessed for quality using the Agilent 2100 Bioanalyzer. Only high-quality samples, determined by the OD260/280 ratio between 1.8 and 2.2, OD260/230 ratio greater than 2.0, RIN value greater than 6.5, 28S:18S ratio greater than 1.0, and RNA quantity exceeding $1\mu\text{g}$, were chosen for constructing the sequencing library. The TruSeq RNA sample preparation kit was employed to build the transcriptome library. Initially, mRNA was selected through the polyA selection method and then fragmented with a fragmentation buffer. The resulting cDNA fragments were then subjected to size selection, where fragments up to 300 bp were selected on a 2% Low Range Ultra agarose gel, followed by PCR amplification with Phusion DNA polymerase (NEB) for 15 cycles. Finally, the sequencing libraries were measured for quantity and quality, then sequenced utilizing the Illumina HiSeq xten/NovaSeq 6000 sequencer with 2×150 bp read length. The free online Majorbio Cloud Platform was used to analyze the data of transcriptomic analysis.

In vitro stimulation of RAW264.7 macrophages with LPS

RAW264.7 macrophages were cultured in 6-well plates for 24 hours. Subsequently, the cells were treated with 100 ng mL^{-1} of LPS and incubated for an additional 24, 48, and 72 hours to evaluate the M2 polarized state using FCM.

Assessment of LGG@Ga-poly combined with LPS in Panc-02 tumor-bearing mice

The mice bearing Panc-02 tumors were divided into two groups: Control and LGG@Ga-poly + LPS (four mice in each group). The mice in the LGG@Ga-poly + LPS group received oral administration of LGG@Ga-poly (5×10^8 CFU) every other day for a total of eleven doses. Simultaneously, LPS ($1\mu\text{g g}^{-1}$) was intraperitoneally injected. At the end of the treatment period, the tumors from both groups were collected for FCM analysis and weight measurement.

In vivo antitumor efficacy of LGG@Ga-poly combined with chemotherapy

In the orthotopic Panc-02 tumor-bearing mice, four groups were formed at random: PBS, Gem, LGG@Ga-poly, and LGG@Ga-poly + Gem (five mice in each group). In the PBS group, $100\mu\text{L}$ PBS was orally administered to mice every two days for a total of eleven times. In the Gem group, Gem (20 mg kg^{-1} per mouse) was intravenously administered on the 0th, 4th, and 8th day. In the LGG@Ga-poly group, LGG@Ga-poly (5×10^8 CFU per mouse) was orally administered every two days for a total of eleven times. In the LGG@Ga-poly + Gem group, Gem (20 mg kg^{-1} per mouse) was intravenously administered on the 0th, 4th, and 8th day, and LGG@Ga-poly (5×10^8 CFU per mouse) was orally administered every two days for a total of eleven times. The mice were sacrificed on Day 28, and tumors were collected for histological analysis.

In vivo antitumor efficacy of LGG@Ga-poly combined with α -PD-L1

The orthotopic Panc-02 tumor-bearing mice were randomly divided into four groups: PBS, α -PD-L1, LGG@Ga-poly, and LGG@Ga-poly + α -PD-L1 (six mice in each group). In the PBS group, $100\mu\text{L}$ of PBS was orally administered to mice every two days for a total of eleven times. In the α -PD-L1 group, α -PD-L1 (0.2 mg per mouse) was intravenously injected on the 0th, 4th, and 8th day. In the LGG@Ga-poly group, LGG@Ga-poly (5×10^8 CFU per mouse) was orally administered every two days for a total of eleven times. In the LGG@Ga-poly + α -PD-L1

group, α -PD-L1 (0.2 mg per mouse) was intravenously injected on the 0th, 4th, and 8th day, and LGG@Ga-poly (5×10^8 CFU per mouse) was orally administered every two days for a total of eleven times. The mice were sacrificed on Day 28, and tumors were collected for histological analysis.

In vivo biosafety

The female C57BL/6 mice were randomly assigned into two groups ($n=3$). The mice received $100\mu\text{L}$ PBS, LGG (5×10^8 CFU per mouse), or LGG@Ga-poly (5×10^8 CFU per mouse) via oral administration, respectively. Three days after treatment, blood samples were collected for liver function tests, including ALT, AST, GGT, TP, ALB, and GLO, kidney function tests, including CRE, TBIL, UREA, and GLU, and hematological tests, including WBC, Lymph, Mid, and Gran.

Statistical analysis

The experimental data were analyzed by GraphPad Prism 8 and the significance level was set at $p < 0.05$. Each error bar in the figures represents the standard error of the mean (sem) of at least three independent experiments. Two-tailed Student's t-test was applied to analyze the statistical significance of the difference between two groups, and one-way ANOVA was used for multiple groups. Unless otherwise specified, the mean value was defined as the center value. To minimize bias, the investigators who performed the surgery for cell and in vivo experiments were blinded to the treatment groups.

Reporting summary

Further information on research design is available in the Nature Portfolio Reporting Summary linked to this article.

Data availability

The RNA sequencing data generated in this study have been deposited in the National Center for Biotechnology Information (NCBI) Sequence Read Archive (SRA) database under accession code [PRJNA1042652](#). The 16S rDNA sequencing data generated in this study have been deposited in the NCBI SRA database under accession code [PRJNA1041940](#) and [PRJNA1041943](#). The remaining data are available within the Article, Supplementary Information, or Source Data file. Source data are provided with this paper.

References

- Chen, P. L. et al. Analysis of immune signatures in longitudinal tumor samples yields insight into biomarkers of response and mechanisms of resistance to immune checkpoint blockade. *Cancer Discov.* **6**, 827–837 (2016).
- Darvin, P., Toor, S. M., Nair, V. S. & Elkord, E. Immune checkpoint inhibitors: recent progress and potential biomarkers. *Exp. Mol. Med.* **50**, 1–11 (2018).
- Topalian, S. L., Drake, C. G. & Pardoll, D. M. Immune checkpoint blockade: a common denominator approach to cancer therapy. *Cancer Cell* **27**, 450–461 (2015).
- Patel, S. A. & Minn, A. J. Combination cancer therapy with immune checkpoint blockade: Mechanisms and strategies. *Immunity* **48**, 417–433 (2018).
- Kalbasi, A. & Ribas, A. Tumour-intrinsic resistance to immune checkpoint blockade. *Nat. Rev. Immunol.* **20**, 25–39 (2020).
- Leinwand, J. & Miller, G. Regulation and modulation of antitumor immunity in pancreatic cancer. *Nat. Immunol.* **21**, 1152–1159 (2020).
- Zhao, J. et al. Irreversible electroporation reverses resistance to immune checkpoint blockade in pancreatic cancer. *Nat. Commun.* **10**, 899 (2019).
- Wu, J. C. et al. Oxygen microcapsules improve immune checkpoint blockade by ameliorating hypoxia condition in pancreatic ductal adenocarcinoma. *Bioact. Mater.* **20**, 259–270 (2023).

9. Zhu, Y. et al. CSF1/CSF1R blockade reprograms tumor-infiltrating macrophages and improves response to t-cell checkpoint immunotherapy in pancreatic cancer models. *Cancer Res.* **74**, 5057–5069 (2014).
10. Ho, W. J., Jaffee, E. M. & Zheng, L. The tumour microenvironment in pancreatic cancer-clinical challenges and opportunities. *Nat. Rev. Clin. Oncol.* **17**, 527–540 (2020).
11. Carstens, J. L. et al. Spatial computation of intratumoral T cells correlates with survival of patients with pancreatic cancer. *Nat. Commun.* **8**, 15095 (2017).
12. Yamamoto, K. et al. Autophagy promotes immune evasion of pancreatic cancer by degrading MHC-I. *Nature* **581**, 100–105 (2020).
13. Mayers, J. R. et al. Tissue of origin dictates branched-chain amino acid metabolism in mutant Kras-driven cancers. *Science* **353**, 1161–1165 (2016).
14. Hosein, A. N., Brekken, R. A. & Maitra, A. Pancreatic cancer stroma: an update on therapeutic targeting strategies. *Nat. Rev. Gastroenterol. Hepatol.* **17**, 487–505 (2020).
15. Balachandran, V. P., Beatty, G. L. & Dougan, S. K. Broadening the impact of immunotherapy to pancreatic cancer: Challenges and opportunities. *Gastroenterology* **156**, 2056–2072 (2019).
16. Nejman, D. et al. The human tumor microbiome is composed of tumor type-specific intracellular bacteria. *Science* **368**, 973–980 (2020).
17. Riquelme, E. et al. Tumor microbiome diversity and composition influence pancreatic cancer outcomes. *Cell* **178**, 795–806 (2019).
18. Pushalkar, S. et al. The pancreatic cancer microbiome promotes oncogenesis by induction of innate and adaptive immune suppression. *Cancer Discov.* **8**, 403–416 (2018).
19. Das, S., Shapiro, B., Vucic, E. A., Vogt, S. & Bar-Sagi, D. Tumor cell-derived IL1 beta promotes desmoplasia and immune suppression in pancreatic cancer. *Cancer Res.* **80**, 1088–1101 (2020).
20. Yin, H. et al. Gut-derived lipopolysaccharide remodels tumoral microenvironment and synergizes with PD-L1 checkpoint blockade via TLR4/MyD88/AKT/NF-kappa B pathway in pancreatic cancer. *Cell Death Dis.* **12**, 1033 (2021).
21. Yang, L. et al. Intratumoral microbiota: Roles in cancer initiation, development and therapeutic efficacy. *Sig. Transduct. Target. Ther.* **8**, 35 (2023).
22. Roemhild, R., Bollenbach, T. & Andersson, D. I. The physiology and genetics of bacterial responses to antibiotic combinations. *Nat. Rev. Microbiol.* **20**, 478–490 (2022).
23. Ianiro, G., Tilg, H. & Gasbarrini, A. Antibiotics as deep modulators of gut microbiota: Between good and evil. *Gut* **65**, 1906–1915 (2016).
24. Han, H. et al. Metformin-induced stromal depletion to enhance the penetration of gemcitabine-loaded magnetic nanoparticles for pancreatic cancer targeted therapy. *J. Am. Chem. Soc.* **142**, 4944–4954 (2020).
25. Han, Z.-Y. et al. Inhalable capsular polysaccharide-camouflaged gallium-polyphenol nanoparticles enhance lung cancer chemotherapy by depleting local lung microbiota. *Adv. Mater.* **35**, e2302551 (2023).
26. Zhang, E. et al. Antibacterial metals and alloys for potential biomedical implants. *Bioact. Mater.* **6**, 2569–2612 (2021).
27. Wyszogrodzka, G., Marszałek, B., Gil, B. & Dorozynski, P. Metal-organic frameworks: mechanisms of antibacterial action and potential applications. *Drug Discov. Today* **21**, 1009–1018 (2016).
28. Suez, J., Zmora, N., Segal, E. & Elinav, E. The pros, cons, and many unknowns of probiotics. *Nat. Med.* **25**, 716–729 (2019).
29. McQuade, J. L., Daniel, C. R., Helmink, B. A. & Wargo, J. A. Modulating the microbiome to improve therapeutic response in cancer. *Lancet Oncol.* **20**, E77–E91 (2019).
30. Sanders, M. E., Merenstein, D. J., Reid, G., Gibson, G. R. & Rastall, R. A. Probiotics and prebiotics in intestinal health and disease: From biology to the clinic. *Nat. Rev. Gastroenterol. Hepatol.* **16**, 605–616 (2019).
31. Han, Z.-Y., Chen, Q.-W., Fu, Z.-J., Cheng, S.-X. & Zhang, X.-Z. Probiotic spore-based oral drug delivery system for enhancing pancreatic cancer chemotherapy by gut-pancreas-axis-guided delivery. *Nano Lett.* **22**, 8608–8617 (2022).
32. Saha, M. et al. Microbial siderophores and their potential applications: a review. *Environ. Sci. Pollut. Res.* **23**, 3984–3999 (2016).
33. Si, W. et al. Lactobacillus rhamnosus GG induces cGAS/STING-dependent type I interferon and improves response to immune checkpoint blockade. *Gut* **71**, 521–533 (2022).
34. Song, W. et al. Trapping of lipopolysaccharide to promote immunotherapy against colorectal cancer and attenuate liver metastasis. *Adv. Mater.* **30**, e1805007 (2018).
35. Sethi, V. et al. Gut microbiota promotes tumor growth in mice by modulating immune response. *Gastroenterology* **155**, 33–37 (2018).
36. del Castillo, E. et al. The microbiomes of pancreatic and duodenum tissue overlap and are highly subject specific but differ between pancreatic cancer and noncancer subjects. *Cancer Epidemiol. Biomarkers* **28**, 370–383 (2019).
37. Velkov, T., Roberts, K. D., Nation, R. L., Thompson, P. E. & Li, J. Pharmacology of polymyxins: New insights into an old class of antibiotics. *Future Microbiol.* **8**, 711–724 (2013).
38. Han, X. et al. Reversal of pancreatic desmoplasia by re-educating stellate cells with a tumour microenvironment-activated nanosystem. *Nat. Commun.* **9**, 3390 (2018).
39. Mayneris-Perxachs, J. & Maria Moreno-Navarrete, J. & Manuel Fernandez-Real, J. The role of iron in host-microbiota crosstalk and its effects on systemic glucose metabolism. *Nat. Rev. Endocrinol.* **18**, 683–698 (2022).
40. Kelson, A. B., Carnevali, M. & Truong-Le, V. Gallium-based anti-infectives: Targeting microbial iron-uptake mechanisms. *Curr. Opin. Pharmacol.* **13**, 707–716 (2013).
41. Kramer, J., Özkaya, Ö. & Kümmerli, R. Bacterial siderophores in community and host interactions. *Nat. Rev. Microbiol.* **18**, 152–163 (2020).
42. Lee, Y. et al. Hyaluronic acid-bilirubin nanomedicine for targeted modulation of dysregulated intestinal barrier, microbiome and immune responses in colitis. *Nat. Mater.* **19**, 118–126 (2020).
43. Ochi, A. et al. MyD88 inhibition amplifies dendritic cell capacity to promote pancreatic carcinogenesis via Th2 cells. *J. Exp. Med.* **209**, 1671–1687 (2012).
44. Geller, L. T. et al. Potential role of intratumor bacteria in mediating tumor resistance to the chemotherapeutic drug gemcitabine. *Science* **357**, 1156–1160 (2017).
45. Guenther, M. et al. Bacterial lipopolysaccharide as negative predictor of gemcitabine efficacy in advanced pancreatic cancer-translational results from the AIO-PK0104 Phase 3 study. *Br. J. Cancer* **123**, 1370–1376 (2020).

Acknowledgements

This work was supported by the National Key Research and Development Program of China (2019YFA0905603, X.Z.Z.) and the National Natural Science Foundation of China (51988102, 52333004 and 22135005, X.Z.Z.). Figures 1 and 4n, created with BioRender.com, were released under a Creative Commons Attribution-NonCommercial-NoDerivs 4.0 International license.

Author contributions

Z.Y.H. and X.Z.Z. conceived the project and designed the experiments. Z.Y.H. and Z.J.F. synthesized materials. Z.Y.H. and Z.J.F. performed in vitro microbiological experiments. Z.Y.H., Y.Z.W., J.X.A., and Z.J.F. performed in vitro cell experiments. Z.Y.H., Y.Z.W., J.X.A., and C.Z. performed in vivo experiments. Z.Y.H., Q.W.C., and Z.J.F. collected and analyzed

the data. All authors discussed the results, wrote the manuscript, and reviewed the manuscript.

Competing interests

The authors declare no competing interests.

Additional information

Supplementary information The online version contains supplementary material available at <https://doi.org/10.1038/s41467-024-51534-z>.

Correspondence and requests for materials should be addressed to Xian-Zheng Zhang.

Peer review information *Nature Communications* thanks Federica Facciotti, Ming-Shiou Jan, Min Zhou and the other, anonymous, reviewer(s) for their contribution to the peer review of this work. A peer review file is available.

Reprints and permissions information is available at <http://www.nature.com/reprints>

Publisher's note Springer Nature remains neutral with regard to jurisdictional claims in published maps and institutional affiliations.

Open Access This article is licensed under a Creative Commons Attribution-NonCommercial-NoDerivatives 4.0 International License, which permits any non-commercial use, sharing, distribution and reproduction in any medium or format, as long as you give appropriate credit to the original author(s) and the source, provide a link to the Creative Commons licence, and indicate if you modified the licensed material. You do not have permission under this licence to share adapted material derived from this article or parts of it. The images or other third party material in this article are included in the article's Creative Commons licence, unless indicated otherwise in a credit line to the material. If material is not included in the article's Creative Commons licence and your intended use is not permitted by statutory regulation or exceeds the permitted use, you will need to obtain permission directly from the copyright holder. To view a copy of this licence, visit <http://creativecommons.org/licenses/by-nc-nd/4.0/>.

© The Author(s) 2024